Astronomy & Astrophysics

Bar pattern speeds in CALIFA galaxies

III. Solving the puzzle of ultrafast bars

Virginia Cuomo[1,2], Yun Hee Lee[3], Chiara Buttitta[2], J. Alfonso L. Aguerri[4,5],
Enrico Maria Corsini[2,6], and Lorenzo Morelli[1]

[1] Instituto de Astronomía y Ciencias Planetarias, Universidad de Atacama, Avenida Copayapu 485, Copiapó, Chile
e-mail: virginia.cuomo@uda.cl
[2] Dipartimento di Fisica e Astronomia "G. Galilei", Universit di Padova, vicolo dell'Osservatorio 3, 35122 Padova, Italy
[3] Korea Astronomy and Space Science Institute, 776 Daedeokdae-ro, Yuseong-gu 34055, Daejeon, Korea
[4] Instituto de Astrofísica de Canarias, calle Vía Láctea s/n, 38205 La Laguna, Tenerife, Spain
[5] Departamento de Astrofísica, Universidad de La Laguna, Avenida Astrofísico Francisco Sánchez s/n, 38206 La Laguna, Tenerife, Spain
[6] INAF – Osservatorio Astronomico di Padova, vicolo dell'Osservatorio 2, 35122 Padova, Italy

ABSTRACT

Context. More than 10% of barred galaxies with a direct measurement of the bar pattern speed host an ultrafast bar. These bars extend well beyond the corotation radius and challenge our understanding of the orbital structure of barred galaxies. Most of the bars are found in spiral galaxies, rather than in lenticular galaxies.
Aims. We analyse the properties of the ultrafast bars detected in the Calar Alto Legacy Integral Field Spectroscopy Area Survey to investigate whether they are an artefact resulting from an overestimation of the bar radius and/or an underestimation of the corotation radius or a new class of bars, whose orbital structure has not been understood yet.
Methods. We revised the available measurements of the bar radius based on ellipse fitting and Fourier analysis and of the bar pattern speed from the Tremaine-Weinberg method. In addition, we measured the bar radius from the analysis of the maps tracing the transverse-to-radial force ratio, which we obtained from the deprojected *i*-band images of the galaxies retrieved from the Sloan Digital Sky Survey.
Results. We found that nearly all the sample galaxies are spirals with an inner ring or pseudo-ring circling the bar and/or with strong spiral arms, which hamper the measurement of the bar radius from the ellipse fitting and Fourier analysis. According to these methods, the bar ends overlap with the ring or the spiral arms, thereby making the adopted bar radius unreliable. On the contrary, the bar radius from the ratio maps are shorter than the corotation radius. This agrees with the theoretical predictions and findings of numerical simulations regarding the extension and stability of the stellar orbits supporting the bars.
Conclusions. We conclude that ultrafast bars are no longer observed when the correct measurement of the bar radius is adopted. Deriving the bar radius in galaxies with rings and strong spiral arms is not straightforward and a solid measurement method based on both photometric and kinematic data is still missing.

Key words. galaxies: kinematics and dynamics – galaxies: structure – galaxies: formation – galaxies: evolution – galaxies: fundamental parameters

1. Introduction

Many disc galaxies, including the Milky Way, host a central bar that contains up to ~30% of the total light (Marinova & Jogee 2007; Barazza et al. 2008; Aguerri et al. 2009; Bland-Hawthorn & Gerhard 2016). This structure forms from internal or externally induced dynamical instabilities in a differentially rotating stellar disc and tumbles around the galaxy centre (Sellwood 1981; Noguchi 1988; Friedli 1999; Martinez-Valpuesta et al. 2017).

Three main properties allow us to fully describe a bar: its radius, strength, and pattern speed (e.g. Aguerri et al. 2015). The bar radius and strength can be derived by analysing optical or near-infrared images, while the bar pattern speed is a dynamical parameter that requires kinematic measurements. The bar radius R_{bar} is defined as the length of the bar semi-major axis and measures the extension of the stellar orbits supporting the bar (Contopoulos & Papayannopoulos 1980; Contopoulos 1981). However, bars do not usually present sharp edges and are often associated with other components such as rings and/or spiral

arms, so it is difficult to properly identify the bar boundaries (Aguerri et al. 2009). In turn, the presence of a large bulge complicates the analysis (Aguerri et al. 2005). Several methods have been developed to derive R_{bar}, but each of these approaches suffers from some limitations (see e.g. Corsini 2011, for a discussion). In order to overcome the problems related to the choice of a single method, usually R_{bar} is estimated by combining the results of various independent methods (Corsini et al. 2003; Guo et al. 2019; Cuomo et al. 2020). The bar strength S_{bar} describes the contribution given by the fnon-axisymmetric mass density of the bar to the galaxy gravitational potential (Buta et al. 2001) and this value can be used to distinguish between strong and weak bars (Cuomo et al. 2019a). The results based on the strength of bars are somewhat controversial because S_{bar} strongly depends on the method used to measure this value (Lee et al. 2020). The bar pattern speed Ω_{bar} is the angular frequency of the bar tumbling around the galaxy centre and determines the so-called corotation radius R_{cr}, which is the radius where the angular velocity of the disc V_{circ} is equal to Ω_{bar}. Bars can be classified

according to the rotation rate parameter, defined as $\mathcal{R} = R_{cr}/R_{bar}$ (Elmegreen 1996).

Bars are mainly supported by elongated stellar orbits called x_1 orbits, which are stable within R_{cr}. In contrast, x_1 orbits outside R_{cr} are arranged perpendicular to the bar major axis and do not sustain the bar structure (Contopoulos & Papayannopoulos 1980; Contopoulos 1981; Vasiliev & Athanassoula 2015). Current dynamical arguments show that bars cannot have $\mathcal{R} < 1.0$. On the other hand, bars with $\mathcal{R} \geq 1.0$ are usually classified either as fast ($1.0 \leq \mathcal{R} \leq 1.4$) or slow ($\mathcal{R} > 1.4$). Fast bars end close to corotation and rotate as fast as they can, while slow bars are shorter and rotate more slowly. The separation between long (or fast) and short (or slow) bars does not imply a specific value of Ω_{bar}, while the dividing value at 1.4 is commonly used (Athanassoula 1992; Debattista & Sellwood 2000). The definition of $\mathcal{R}$ was introduced by Elmegreen (1996) to show how bars usually end inside corotation, possibly between the ultraharmonic 4:1 resonance and corotation. However, the bar-spiral transition does not occur at corotation and the spiral arms can extend for a significant distance inside corotation, since spiral density waves can propagate between the inner and outer Lindblad resonances (Adams et al. 1989; Bertin & Lin 1996).

As a consequence of the angular momentum exchange within the galaxy and of the dynamical friction exerted on the bar by the dark matter (DM) halo, Ω_{bar} is expected to decrease with time during the evolution (Weinberg 1985; Little & Carlberg 1991; Debattista & Sellwood 1998; O'Neill & Dubinski 2003; Villa-Vargas et al. 2010; Athanassoula et al. 2013). The slowdown of the bar is stronger if a massive and centrally concentrated DM halo is present, because there is more mass ready to absorb angular momentum near the resonances and dynamical friction is more efficient (see Athanassoula 2014 and Sellwood 2014, for further discussion). This implies that galaxies hosting fast bars should be embedded in DM haloes with a low central density, such as those required in the maximum disc hypothesis (Debattista & Sellwood 2000; Palunas & Williams 2000; Fuchs 2001; Starkman et al. 2018). Nevertheless, other galaxy properties, such as halo triaxiality, presence of gas, and disc velocity dispersion, may influence the angular momentum exchange within the galaxy (Athanassoula 2003; Athanassoula et al. 2013). The measurement of $\mathcal{R}$ may help to disentangle the DM distribution and to investigate the secular evolution of barred galaxies.

There are several methods to recover Ω_{bar} and consequently $\mathcal{R}$, but most of these require some modelling (Kormendy 1979; Athanassoula 1992; Lindblad & Kristen 1996; Puerari & Dottori 1997; Aguerri et al. 2000; Zhang & Buta 2007; Rautiainen et al. 2008; Font et al. 2011). Tremaine & Weinberg (1984) developed a technique to recover Ω_{bar}, hereafter called TW method, which does not require any dynamical model. When the bar is characterised by an exact solid-body rotation, Ω_{bar} is directly determined from observable quantities measured for a tracer population of stars or gas, which only has to satisfy the continuity equation. This method requires measurement of the surface brightness and radial velocity of the tracer along apertures located parallel to the line of nodes. When both positions and velocities are measured with respect to the galaxy centre, then the luminosity-weighted mean velocity divided by the luminosity-weighted mean position gives $\Omega_{bar} \sin i$, where i is the disc inclination.

More than 100 galaxies have been analysed with the TW method so far, each providing an estimate for $\mathcal{R}$ (see Cuomo et al. 2020, for a review). Neglecting measurements with large uncertainties, ~90% of the bars are consistent with the fast regime at

95% confidence level. These galaxies should host little DM in their central regions, which agrees with the findings based on the study of rotation curves for unbarred galaxies (Debattista & Sellwood 2000; Starkman et al. 2018).

Despite theoretical predictions, ~10% of the galaxies with Ω_{bar} measured with the TW method shows $\mathcal{R} < 1.0$ at 95% confidence level: these bars are termed ultrafast (Buta & Zhang 2009). According to the Calar Alto Legacy Integral Field Spectroscopy Area Survey (CALIFA; Sánchez et al. 2012; Walcher et al. 2014; Falcón-Barroso et al. 2017) morphological classification, with the exception of the lenticular galaxy NGC 2880 (Cuomo et al. 2020), all of these bars are found in late-type barred galaxies with Hubble stage T between 2 and 7. Whether ultrafast bars are the consequence of an erroneous application of the TW method or a special class of bars, which do not obey to the predictions of theory and numerical simulations (see Aguerri et al. 2015 and Guo et al. 2019, for a discussion). However, a non-negligible fraction of ultrafast bars was also observed while applying other methods (Buta & Zhang 2009; Buta 2017). Garma-Oehmichen et al. (2020) analysed the different sources of error in the TW method and quantified how much these errors affect the final measurement of Ω_{bar} in a sample of 15 galaxies. The dominant sources of error are the identification of the disc position angle (PA) and the length of the apertures along which to measure the position and velocity of the tracer, while centring errors and a degraded point-spread-function result in a small or negligible effect. Garma-Oehmichen et al. (2020) do not observe a significant correlation between the error sources, but they stress the importance of the correct error treatment. They claim that a large fraction of ultrafast bars may be the result of an erroneous treatment of the errors together with low spatial resolution data. New studies are needed to eventually exclude that these results are flawed because of an improper application of the TW method and/or to investigate if some information about the nature of ultrafast bars is still missing.

Recent studies point out that spiral arms may affect the measurement of R_{bar} (Petersen et al. 2019; Hilmi et al. 2020). In particular, Hilmi et al. (2020) show with their simulations that the measurement of R_{bar} dramatically fluctuates on a dynamical timescale depending on the strength of the spiral structure and on the measurement threshold. In this paper, we aim to test whether the measurements of R_{bar} adopted in literature may be biased by the presence of the spiral arms or other components, which caused the extremely low values of $\mathcal{R}$.

We organise the paper as follows: We introduce the sample of galaxies and their properties as available in literature in Sect. 2. We present our analysis in Sect. 3. We discuss our results and present our conclusions in Sects. 4 and 5, respectively. We adopt as cosmological parameters, $\Omega_m = 0.286$, $\Omega_\Lambda = 0.714$, and $H_0 = 69.3 \, \text{km s}^{-1} \, \text{Mpc}^{-1}$ (Hinshaw et al. 2013).

2. Sample selection and available data

We considered the 31 barred galaxies studied by Aguerri et al. (2015) and Cuomo et al. (2019a), for which a direct TW measurement of Ω_{bar} was obtained by analysing the stellar kinematics from CALIFA. Aguerri et al. (2015) selected 15 strongly barred galaxies, while Cuomo et al. (2019a) focussed their attention on 16 weakly barred galaxies. The resulting sample spans a wide range of morphological types (SB0 – SBd), redshifts (0.005 – 0.02), and absolute Sloan Digital Sky Survey (SDSS; Abazajian et al. 2009) r-band magnitudes (−18.5 to −22.0 mag). These distributions are similar to those of the total sample of bright barred galaxies targeted by the CALIFA survey. Twelve
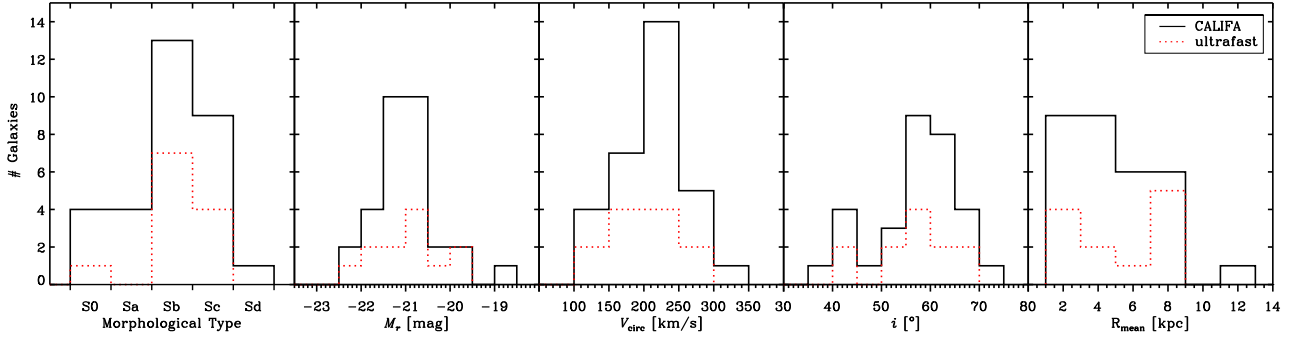
Fig. 1. Distribution of the morphological types, absolute SDSS r-band magnitudes, circular velocities, disc inclinations, and bar radii of the initial sample of 31 CALIFA galaxies analysed with the TW method by Aguerri et al. (2015) and Cuomo et al. (2019a) (black solid line) and of the subsample of 12 galaxies hosting an ultrafast bar discussed in this paper (red dotted line).

galaxies measured by Aguerri et al. (2015) and Cuomo et al. (2019a) host an ultrafast bar, according to their values of $\mathcal{R}$ and corresponding errors. Figure 1 shows the distributions of morphological types, absolute SDSS r-band magnitudes, circular velocities, disc inclinations, and bar radii of the initial sample of 31 galaxies compared to those of the subsample of 12 galaxies hosting an ultrafast bar. We ran a Kolmogorov–Smirnov test with the IDL procedure KSTWO and verified there are no statistical differences at a very high confidence level (>95%) between the distributions of properties of the two samples. All the ultrafast bars except for one are found in SBab−SBc spiral galaxies.

The TW method was applied to recover Ω_{bar} (and consequently $\mathcal{R}$) by using the following straightforward equation:

$$\langle V \rangle = \langle X \rangle \, \Omega_{bar} \, \sin i, \tag{1}$$

which requires to know the disc inclination i,

$$\langle X \rangle = \frac{\int X \Sigma dX}{\int \Sigma dX}, \quad \text{and} \quad \langle V \rangle = \frac{\int V_{los} \Sigma dX}{\int \Sigma dX}, \tag{2}$$

which are defined as the luminosity-weighted average of position X and line-of-sight (LOS) velocity V_{los} of the stars, respectively, where Σ is the surface brightness. These integrals are measured along several pseudo-slits. One pseudo-slit is centred on the galaxy centre and the others have an offset, but all of these are aligned with the disc major axis, which requires the determination of the disc PA.

As described in Aguerri et al. (2015) and Cuomo et al. (2019a), the disc parameters (i and PA) are obtained by analysing the outer isophotes of the galaxy and the resulting radial profiles of the ellipticity ϵ and PA. The galaxy isophotes were modelled using the ELLIPSE routine of the IRAF[1] package (Jedrzejewski 1987).

The slope of the straight line defined by the integrals in Eq. (2) gives $\Omega_{bar} \sin i$. In practice, the luminosity-weighted photometric and kinematic integrals are obtained by collapsing the spectroscopic data cube along the wavelength and spatial directions of each pseudo-slit, respectively. For the sample galaxies, we adopted the values of Ω_{bar} obtained in this way by Aguerri et al. (2015, see Col. 4 in their Table 3) and Cuomo et al. (2019a, see Col. 3 in their Table 2). As an alternative, the kinematic integrals can be directly obtained from the stellar velocity

field. Moreover, either a map of the stellar surface brightness (Aguerri et al. 2015; Guo et al. 2019; Garma-Oehmichen et al. 2020) or stellar surface mass density (Aguerri et al. 2015; Guo et al. 2019; Williams et al. 2021) can be used as a weight in the definition of the integrals. However, the mass and light distributions do not often match well, particularly in the presence of ongoing star formation, as is usually the case in spiral galaxies.

The radius of R_{bar} is usually obtained as the mean value of various measurements retrieved using several methods (Corsini et al. 2003; Cuomo et al. 2019b; Guo et al. 2019). Three different methods were adopted in Aguerri et al. (2015) and Cuomo et al. (2019a) to recover R_{bar} based on the photometric analysis of SDSS images. Hereafter, we refer to this estimate as R_{mean}.

The first two methods are based on the study of the radial profile of ϵ and PA of the ellipses that best fit the galaxy isophotes (Menéndez-Delmestre et al. 2007; Aguerri et al. 2009). The bar radius corresponds to the position of the peak in the ellipticity profile, $R_{\epsilon,peak}$, or to the position where the PA changes by $\Delta PA = 5°$ from the PA of the ellipse with the maximum ϵ value, R_{PA}. Undisturbed barred galaxies usually show a local peak and a sudden outward decrease of ϵ to a minimum value ($\Delta \epsilon \geq 0.08$), which corresponds to the region of the disc where the isophotes become circular in the face-on case (Wozniak & Pierce 1991; Athanassoula 1992; Aguerri et al. 2000). On the other hand, the radial profile of PA is constant in the bar region ($\Delta PA \leq 20°$) (Wozniak & Pierce 1991; Aguerri et al. 2000). These peculiarities are due to the shape and orientation of the stellar orbits of the bar (Contopoulos & Grosbol 1989; Athanassoula 1992). These methods however require calibration on mock galaxy images to set the maximum variation of each isophotal parameter that constrains the corresponding R_{bar}. The third adopted approach to measure R_{bar} consists in the Fourier decomposition of the galaxy light and in the analysis of the bar/inter-bar intensity ratio and provides $R_{Fourier}$ (Ohta et al. 1990; Aguerri et al. 2000). The deprojected azimuthal radial profile of the luminosity of the galaxy $I(r, \phi)$ can be described with a Fourier series

$$I(r, \phi) = \frac{A_0(r)}{2} + \sum_{m=1}^{\infty} [A_m(r) \cos(m\phi) + B_m(r) \sin(m\phi)], \tag{3}$$

where the Fourier components are defined by

$$A_m(r) = \frac{1}{\pi} \int_0^{2\pi} I(r, \phi) \cos(m\phi) d\phi \tag{4}$$

$$B_m(r) = \frac{1}{\pi} \int_0^{2\pi} I(r, \phi) \sin(m\phi) d\phi, \tag{5}$$

---

[1] Image Reduction and Analysis Facility is distributed by the National Optical Astronomy Observatories, which are operated by the Association of Universities for Research in Astronomy under cooperative agreement with the National Science Foundation.

Table 1. Properties of the sample barred galaxies hosting an ultrafast bar.

Galaxy	Morph. type	Hubble type	z	M_r [mag]	i [°]	PA [°]	R_{mean} [arcsec]	Ω_{bar} [km s^{-1} arcsec^{-1}]	R_{cr} [arcsec]	$\mathcal{R}$	Ref.
(1)	(2)	(3)	(4)	(5)	(6)	(7)	(8)	(9)	(10)	(11)	(12)
IC 1528	SABbc	SAB(rs)b	0.013	−20.57	66.7	72.7	$8.89^{+2.73}_{-2.93}$	21.0 ± 3.8	6.74 ± 2.11	$0.76^{+0.14}_{-0.22}$	2
IC 1683	SABb	S?	0.016	−20.73	54.3	13.0	$27.39^{+1.93}_{-2.03}$	9.7 ± 0.4	19.72 ± 8.47	0.72 ± 0.21	2
IC 5309	SABc	Sb	0.014	−19.99	60.0	26.7	$7.39^{+3.32}_{-1.87}$	24.3 ± 7.5	4.67 ± 3.77	$0.63^{+0.35}_{-0.45}$	2
NGC 36	SBb	SAB(rs)b	0.020	−21.86	57.2	23.4	$20.19^{+5.09}_{-4.51}$	17.4 ± 5.2	$12.60^{+5.39}_{-3.91}$	$0.6^{+0.3}_{-0.2}$	1
NGC 2553	SABab	S?	0.016	−21.23	54.6	67.0	$22.16^{+5.97}_{-5.22}$	23.6 ± 1.7	11.40 ± 2.63	$0.51^{+0.08}_{-0.11}$	2
NGC 2880	EAB7	SB0$^-$	0.005	−20.34	56.7	144.6	$12.77^{+6.09}_{-3.60}$	22.2 ± 1.3	9.43 ± 3.09	$0.74^{+0.15}_{-0.19}$	2
NGC 5205	SBbc	S?	0.006	−19.65	50.0	170.1	$17.69^{+2.83}_{-2.07}$	15.1 ± 2.8	$11.34^{+2.99}_{-2.53}$	$0.7^{+0.2}_{-0.1}$	1
NGC 5406	SBb	SAB(rs)bc	0.018	−22.25	44.9	111.8	$21.00^{+1.09}_{-2.10}$	22.8 ± 8.0	$11.01^{+4.80}_{-3.00}$	$0.5^{+0.2}_{-0.1}$	1
NGC 5947	SBbc	SBbc	0.020	−21.28	44.6	72.5	$10.91^{+1.29}_{-1.60}$	31.7 ± 4.2	$5.79^{+2.39}_{-2.30}$	0.5 ± 0.2	1
NGC 5971	SABb	Sa	0.011	−20.57	69.0	132.0	$23.85^{+20.10}_{-10.91}$	16.9 ± 4.3	13.37 ± 6.44	$0.56^{+0.15}_{-0.32}$	2
NGC 6497	SBab	SB(r)b	0.010	−21.72	60.9	112.0	$14.70^{+2.09}_{-1.29}$	42.7 ± 7.4	$5.49^{+2.09}_{-1.60}$	0.3 ± 0.1	1
UGC 3253	SBb	SB(r)b	0.014	−20.65	56.8	92.0	$15.81^{+1.29}_{-2.20}$	15.5 ± 3.1	$11.89^{+3.18}_{-2.69}$	$0.7^{+0.2}_{-0.2}$	1

Notes. (1) Galaxy name. (2) Morphological classification from CALIFA (Walcher et al. 2014). (3) Hubble type from de Vaucouleurs et al. (1991, hereafter RC3). (4) Redshift from SDSS-DR14 (Abolfathi et al. 2018). (5) Absolute SDSS r-band magnitude obtained from the model r-band apparent magnitude m_r provided by the SDSS-DR14 and the galaxy distance from NED (The NASA/IPAC Extragalactic Database is available at https://ned.ipac.caltech.edu/) as obtained from the radial velocity with respect to the cosmic microwave background reference frame. (6) Disc inclination. (7) Disc PA. (8) Deprojected bar radius. (9) Bar pattern speed. (10) Bar corotation radius. (11) Bar rotation rate. (12) Source of disc and bar properties: 1 = Aguerri et al. (2015), 2 = Cuomo et al. (2019a).

and the Fourier amplitude of the m-th component is defined as

$$I_m(r) = \begin{cases} A_0(r)/2 & \text{if } m = 0 \\ \sqrt{A_m^2(r) + B_m^2(r)} & \text{if } m \neq 0. \end{cases} \qquad (6)$$

In the bar region, the relative amplitudes I_m/I_0 of the even Fourier components ($m = 2, 4, 6, \ldots$) are larger than the odd amplitudes ($m = 1, 3, 5, \ldots$), and the dominant amplitude is $m = 2$. Through this analysis, R_{Fourier} can be recovered from the luminosity contrast between the bar and inter-bar intensity as a function of radial distance (Aguerri et al. 2000). The intensity of the bar is defined as $I_{\mathrm{bar}} = I_0 + I_2 + I_4 + I_6$, while that of the inter-bar is defined as $I_{\mathrm{ibar}} = I_0 - I_2 + I_4 - I_6$. The bar region is where the bar/inter-bar intensity ratio $I_{\mathrm{bar}}/I_{\mathrm{ibar}} > 0.5 \times [\max(I_{\mathrm{bar}}/I_{\mathrm{ibar}}) - \min(I_{\mathrm{bar}}/I_{\mathrm{ibar}})] + \min(I_{\mathrm{bar}}/I_{\mathrm{ibar}})$ and R_{Fourier} corresponds to the full width at half maximum (FWHM) of the curve given by $I_{\mathrm{bar}}/I_{\mathrm{ibar}}$ as a function of radius. This method was tested with N-body simulations resulting to provide an error of 4% on the corresponding R_{bar} (Athanassoula & Misiriotis 2002). However, the application of this method can be hampered by the presence of a non-axisymmetric disc and strong spiral arms.

The bar rotation rate $\mathcal{R}$ is obtained as the ratio of R_{cr} to R_{bar}. In turn, R_{cr} is given by the ratio of Ω_{bar} to V_{circ}, which is usually estimated with an asymmetric drift correction of the observed stellar streaming velocities (Merrifield & Kuijken 1995; Debattista et al. 2002a; Aguerri et al. 2015; Cuomo et al. 2019a). In our analysis, the bar is not only considered to be ultrafast if the corresponding $\mathcal{R}$ is lower than 1.0 at 95% confidence level (as done in Cuomo et al. 2020), but when the sum between $\mathcal{R}$ and its upper error is lower than 1.0. This choice allows us to build a better defined sample of possible ultrafast bars. The corresponding sample consists of 12 galaxies with properties presented in Table 1 and corresponding SDSS colour images given in Fig. 2.

3. Revising the determination of the bar rotation rate

The determination of $\mathcal{R}$ involves two different quantities that characterise the bar: its radius and the corotation radius. For our sample, the determination of R_{cr} was obtained with the TW method, so the corresponding sources of error have to be considered. On the other hand, R_{bar} was calculated using multiple methods based on photometry, which may be affected by their own limitations.

3.1. Sources of error for the TW analysis

The successful application of the TW method requires the disc to have an intermediate i and the bar to be located at an intermediate PA with respect to the disc major and minor axes (Corsini 2011). Moreover, recovering bar PA and ϵ from ellipse fitting can be very difficult when the galaxy is very inclined (Comerón et al. 2014). All the sample galaxies were selected to have an inclination $20° \lesssim i \lesssim 70°$ and a PA difference between bar and disc major axis $10° \lesssim \Delta\mathrm{PA} \lesssim 80°$.

Cuomo et al. (2020) explore the relative errors on Ω_{bar}, R_{bar}, and R_{cr} for all the galaxies with available TW measurements as a function of the disc i and bar ΔPA, respectively (see their Figs. 2 and 3). They did not observe any significant trend and excluded any selection bias on the entire galaxy sample. This result is true for the subsample of galaxies hosting an ultrafast bar as well.

Moreover, the right identification of the disc parameters (especially the PA along which to locate the pseudo-slits) is crucial for the TW method (Debattista 2003; Zou et al. 2019). All the galaxies were carefully selected to be suitable for the TW analysis because they present a constant behaviour of the PA radial profile in the disc region. Moreover, the sources of error associated with the TW method–that is uncertainties in the identification of the disc PA and galaxy centre and in the choice of the length of the pseudo-slits (Corsini 2011; Garma-Oehmichen et al. 2020)–were fully taken into account in the application of the TW method and propagated in the error estimate of Ω_{bar}.
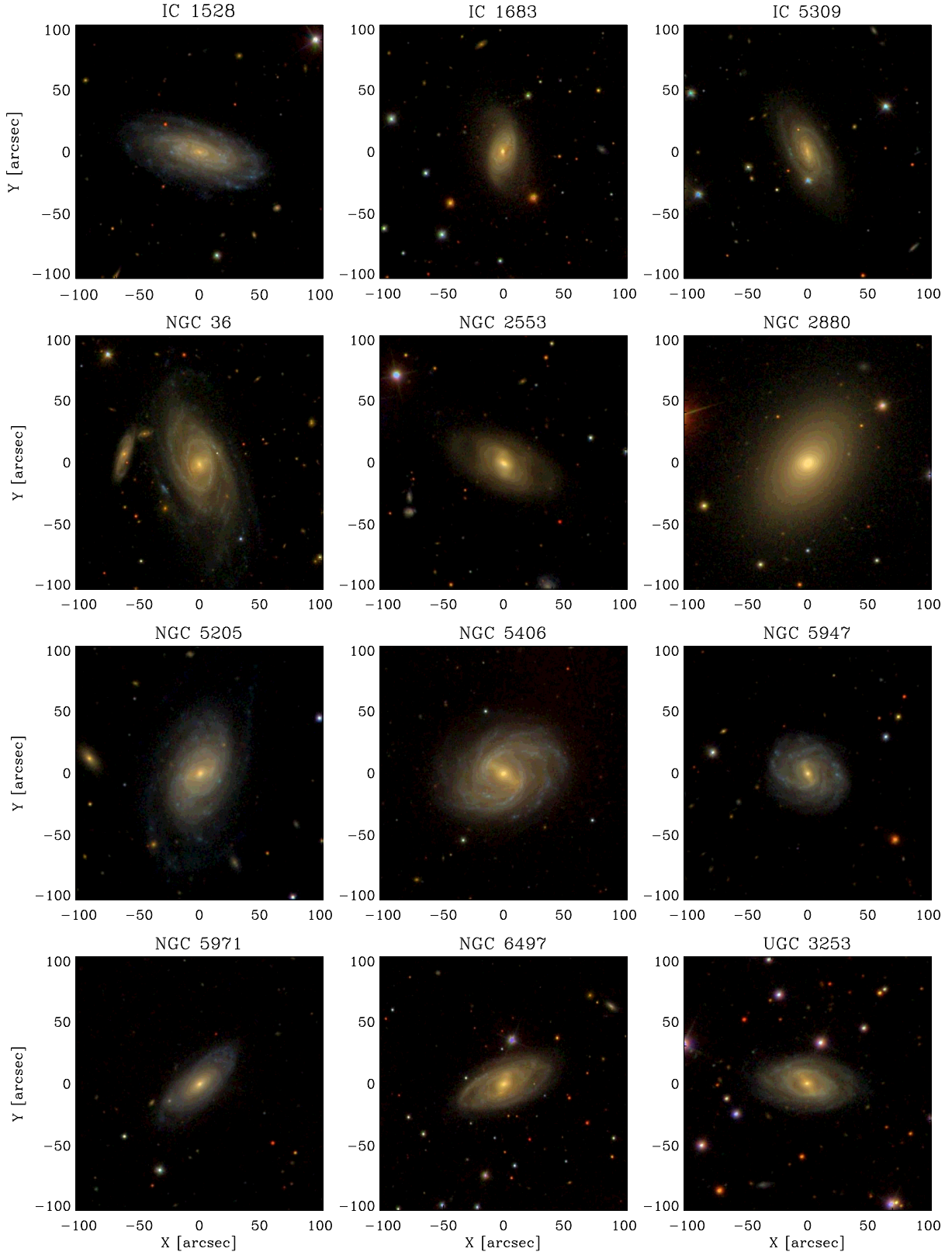
Fig. 2. SDSS colour images of the sample galaxies. The field of view is $100 \times 100 \, \text{arcsec}^2$ and it is orientated with north up and east left.

3.2. Considerations about galaxy morphology

In the early application of the TW method, mainly lenticular galaxies were targeted. This was done to face the strict requests of the method, the limitations due to the long-slit spec-troscopy, and to avoid morphological peculiarities or multiple pattern speeds that may be associated with spiral arms. After the primary adoption of integral-field spectroscopy and the availability of more theoretical studies about the impact of multiple spiral arms on the TW analysis (Debattista et al. 2002a;

Meidt et al. 2008), spiral galaxies were measured and a non-negligible fraction of ultrafast bars were found in these galaxies. In the initial sample of 31 CALIFA galaxies, 11 out of 27 SBa – SBd galaxies (41%) host an ultrafast bar, while this is the case only for 1 out of 4 SB0s (25%). The presence of spiral arms and other structures makes it more difficult to correctly determine the disc parameters and TW integrals (Corsini 2011; Cuomo et al. 2020). Nevertheless, the applicability of the TW method to spiral galaxies was tested and demonstrated by both theoretical (Gerssen & Debattista 2007; Zou et al. 2019) and observational studies involving high quality integral-field data (Aguerri et al. 2015; Guo et al. 2019; Garma-Oehmichen et al. 2020; Williams et al. 2021). In particular, Gerssen & Debattista (2007) explored the possible influence of the presence of dust on the reliable application of the TW method. In addition, Aguerri et al. (2015) used the distribution of the mass as weight for the integrals, and they found that the results are compatible with the case of light as weight. In particular, they discussed the cases of NGC 36, NGC 5205, and NGC 6947, excluding that the presence of dust may lead to a value of $\mathcal{R} < 1.0$.

We carefully performed a visual inspection of the colour images of the galaxies showed in Fig. 2 and inspected the SDSS $g - i$ colour images before and after their deprojection. We concluded that most of the galaxy in our sample (7 out of 12, corresponding to ~60%) host inner rings or pseudo-rings around the bar. Three of these also present an outer ring or pseudo-ring. These structures are often associated with a pronounced light deficit around the bar inside the inner ring, giving rise to a typical "θ" shape, called a dark gap (Kim et al. 2016; James & Percival 2016; Buta 2017). This is the case for the galaxies NGC 36, NGC 2553, NGC 5205, NGC 5406, NGC 5947, NGC 6497, and UGC 3253 (Fig. 2). We carefully analysed those features using the prescriptions of Buta et al. (2015), Buta (2017), and Bittner et al. (2020). Multiple spiral arms are clearly visible in most of the sample galaxies except for IC 1683 and NGC 2553, which host a two-armed structure, as well as NGC 2880, which does not host any spiral arm and is a lenticular galaxy. Flocculent spiral arms are clearly visible in IC 1528, NGC 5406, and NGC 5947, while grand-design spiral arms are visible in IC 5309 and NGC 36. We concluded that our sample galaxies host spiral arms with various geometrical properties, such as level of symmetry, and amplitude, spanning from flocculent, to multi-armed and grand-design morphologies. The results of our morphological analysis are presented in Sect. 3.5 for the entire galaxy sample.

3.3. Errors in bar radius

The adopted values of R_{bar} for the sample galaxies, R_{mean}, correspond to the mean result obtained using three different methods based on photometry. However, several issues may lead to the wrong determination of R_{bar}. In particular, a late-type morphology that includes the presence of strong spiral arms or other structures may hamper the right determination of R_{bar} (Petersen et al. 2019; Hilmi et al. 2020).

To obtain an independent method to recover R_{bar}, we applied the method proposed by Lee et al. (2020) based on the analysis of the maps tracing the transverse-to-radial force ratio $Q_T(r, \phi)$ of the galaxy (Sanders & Tubbs 1980; Combes & Sanders 1981). While all the other methods discussed in Sect. 2 are based on the study of the light distribution in galaxies, the approach proposed by Lee et al. (2020) involves the calculation of the gravitational potential of the galaxy expected from the light

distribution. Even though this method is also based on photometry, this method allows us to obtain an independent R_{bar} estimate, which we call R_{Qb} hereafter. In particular, the method allows us to disentangle the radius corresponding to the maximum strength of the bar from that of the spiral arms and/or rings by investigating the azimuthal profile according to the radius and to test whether R_{mean} truly matches the bar region. At the same time, using this method we obtain an alternative estimate of S_{bar}, hereafter called Q_b.

After deprojecting the SDSS i-band image of the galaxy, the Poisson equation is solved assuming a constant mass-to-light ratio. The gravitational potential is obtained from the Poisson equation by the convolution of the three-dimensional mass density $\rho(\mathbf{x}')$ and $1/|\mathbf{x} - \mathbf{x}'|$ (Quillen et al. 1994; Buta & Block 2001)

$$\Psi(\mathbf{x}) = -G \int \frac{\rho(\mathbf{x}')\mathrm{d}^3\mathbf{x}'}{|\mathbf{x} - \mathbf{x}'|}. \tag{7}$$

The three-dimensional mass density can be written as $\rho(\mathbf{x}') = \Sigma(x, y)\rho_z(z)$, where $\Sigma(x, y)$ is the mass surface density in the plane of the galaxy and $\rho_z(z)$ is the normalised vertical density distribution assumed to follow an exponential profile. In the galaxy plane $z = 0$, the two-dimensional potential can be defined in polar coordinates $\Phi(r, \phi) \equiv \Psi(x, y, z = 0)$.

The mean radial force $\langle F_R(r) \rangle$ and transverse force $F_T(r, \phi)$ can be defined as

$$\langle F_R(r) \rangle \equiv \frac{\mathrm{d}\Phi_0(r)}{\mathrm{d}r}, \quad \text{and} \quad F_T(r, \phi) \equiv \left| \frac{1}{r} \frac{\partial \Phi(r, \phi)}{\partial \phi} \right|, \tag{8}$$

where Φ_0 is the $m = 0$ Fourier component of the gravitational potential (Buta & Block 2001). The maximum transverse force to the mean radial force is defined as

$$Q_T(r) \equiv \frac{F_T^{max}(r)}{\langle F_R(r) \rangle}, \tag{9}$$

where the maximum tangential force $F_T^{max}(r)$ is the maximum of $F_T(r, \phi)$ along ϕ. The ratio map $Q_T(r, \phi)$ of a barred galaxy typically presents four thick slabs and the four peaks along these slabs are observed near to the four corners of the bar in the deprojected image of the galaxy (see Fig. 1 in Lee et al. 2020). The ratio map can also be expressed in Cartesian coordinates $Q_T(x, y)$, where a butterfly-shaped pattern is the typical signature of the presence of a bar.

The radial profile of Q_T is calculated to be averaged over the azimuthal angle ϕ (Buta & Block 2001). The analysis of the shape of the $\langle Q_T \rangle$ radial profile allows us to constrain the bar radius. The location of a peak or a plateau in the $\langle Q_T \rangle$ radial profile is adopted as a solid estimate of the bar radius, R_{Qb}. At this radius, four peaks appear in the $Q_T(R_{Qb})$ azimuthal profile confirming the correct identification of the bar.

The method was originally proposed to perform a morphological classification because the specific characteristics of the $\langle Q_T \rangle$ radial and $Q_T(r_{Qb})$ azimuthal profiles allow us to distinguish between barred and unbarred galaxies. In particular, Lee et al. (2020) identify a barred galaxy when the $Q_T(R_{Qb})$ azimuthal profile presents four peaks corresponding to the four wings of the butterfly-shaped pattern shown in Buta & Block (2001), together with a global bar strength $Q_b > 0.15$, defined as the bar force ratio in the polar coordinates

$$Q_b \equiv \frac{1}{n} \sum_{i=1}^{n} Q_{T,i}, \tag{10}$$

Table 2. Bar radius R_{Qb} and strength Q_b from the analysis of the transverse-to-radial force ratio map of the sample galaxies.

Galaxy	R_{Qb} [arcsec]	Q_b	Class	$\mathcal{R}_{new}$
(1)	(2)	(3)	(4)	(5)
IC 1683	13.86 ± 3.56	0.28	B	$1.42^{+0.62}_{-0.83}$
IC 5309	7.13 ± 3.56	0.11	NB	$0.65^{+0.47}_{-0.83}$
NGC 36	12.28 ± 2.77	0.33	B	$1.03^{+0.37}_{-0.41}$
NGC 2553	12.68 ± 2.77	0.25	B	$0.90^{+0.18}_{-0.22}$
NGC 2880	9.90 ± 3.17	0.19	B	$0.95^{+0.27}_{-0.39}$
NGC 5205	12.28 ± 3.56	0.29	B	$0.92^{+0.22}_{-0.28}$
NGC 5406	13.86 ± 3.56	0.37	B	$0.79^{+0.29}_{-0.24}$
NGC 5947	8.32 ± 1.98	0.26	B	$0.70^{+0.26}_{-0.30}$
NGC 6497	11.49 ± 2.38	0.34	B	$0.48^{+0.16}_{-0.17}$
UGC 3253	11.88 ± 1.89	0.40	B	$1.00^{+0.27}_{-0.24}$

Notes. (1) Galaxy name. (2) Deprojected bar radius. (3) Bar strength. (4) Barred (B) or unbarred (NB) classification according to Lee et al. (2020) criteria. (5) Bar rotation rate estimated as the ratio of R_{cr} tabulated in Table 1 to R_{Qb} from Col. (2).

where $Q_{T,i}$ is the maximum value at each peak on the $Q_T(R_{Qb})$ azimuthal profile, and n is the number of the peaks which is equal to four for a bar.

First of all, we considered the SDSS i-band images after measuring and subtracting the residual sky level, as done in Morelli et al. (2016). We deprojected the SDSS i-band images using the disc parameters provided by Aguerri et al. (2015) and Cuomo et al. (2019a) and reported in Table 1. To double check if these disc parameters were carefully identified and suitable for the deprojection of the images, we repeated the image deprojection using the disc parameters obtained at the half of the radius of the isophote at a surface brightness level of $\mu_B = 25$ mag arcsec^{-2} ($R_{25}/2$, RC3). This corresponds to the maximum extension of the residual sky-subtracted SDSS images. The two deprojected images provide consistent results in the resulting analysis. We adopted and present in the following the results corresponding to the deprojection based on the data from Aguerri et al. (2015) and Cuomo et al. (2019a).

We recovered an independent measurement of bar radius R_{Qb} and bar strength Q_b, which are tabulated in Table 2. The corresponding error on R_{Qb} was obtained as the width of the peak in the $\langle Q_T \rangle$ radial profile, calculated where $\langle Q_T \rangle$ reaches 95% of the peak value and using only the right side of the profile, since the peak is not always well defined. The results obtained for our sample galaxies are showed in Figs. 3 and A.1 and described in Sect. 3.5. In particular, Fig. 3 shows the analysis of the ratio map for NGC 5406. The original SDSS image, the deprojected image obtained from the disc parameters tabulated in Table 1, and the ratio map as a function of the polar coordinates (r, ϕ) are presented in the upper panels. The four thick slabs corresponding to the bar are visible in the inner part of the map (clearly extending up to $r = 20$ arcsec). Outermost the slabs transform into a more complex pattern, corresponding to the spiral arms. In the lower panels of the figure are presented the $\langle Q_T \rangle$ radial, $Q_T(R_{Qb})$ azimuthal, and $Q_T(R_{mean})$ azimuthal profiles.

The galaxies IC 1528 and NGC 5971 are very inclined so the $Q_T(r, \phi)$ map analysis is not conclusive. In particular, IC 1528 does not present the typical features of a barred galaxy after deprojection, while the bar of NGC 5971 appears as an artefact structure elongated along the disc minor axis due to deprojec-

tion. We decided to discard these galaxies from further analysis of the ratio map and our final sample reduces to 10 objects.

As a first result, we confirmed that all these galaxies host a strong bar, according to the criteria proposed by Lee et al. (2020), except for IC 5309. This galaxy presents the typical four peaks in the $Q_T(R_{Qb})$ azimuthal profile but a lower value of Q_b than the threshold adopted to define a barred galaxy. This allowed us to confirm that it is a weakly barred galaxy, as already pointed out by the visual classification from CALIFA (Walcher et al. 2014) and the analysis from Cuomo et al. (2019a).

Moreover, we tested the value of R_{mean} tabulated in Table 1 to recover $\mathcal{R}$ by analysing the $Q_T(R_{mean})$ azimuthal profile to look for the typical four peaks expected for the bar. We checked where the resulting peaks are located on the galaxy image (see panel b of Figs. 3 and A.1).

We found that $R_{mean} > R_{Qb}$ by ~45% on average and in three galaxies the two values are not even consistent to each other within their errors. In fact, R_{mean} is always larger than R_{Qb} at face values, but the large errors associated with R_{mean} make the two values consistent in many cases. Only for IC 1683, IC 5309, and NGC 2880, R_{mean} corresponds to the bar radius, but it remains larger than R_{Qb} at face values. On the contrary, we realised that R_{mean} for NGC 2553 and NGC 5406 is the radius of the ring circling the bar. The corresponding $Q_T(R_{mean})$ azimuthal profile shows more than the four peaks we expect to have for a bar. For NGC 36, NGC 5205, NGC 5947, NGC 6497, and UGC 3253, the $Q_T(R_{mean})$ azimuthal profile shows four peaks but the value of R_{mean} corresponds to a galactocentric distance at which a ring or spiral arms are clearly visible in the galaxy image. A detailed description of the morphology of the sample galaxies with a comparison between R_{mean} and R_{Qb} is presented in Sect. 3.5.

We calculated $\mathcal{R}$ by dividing the value of R_{cr} tabulated in Table 1 by R_{Qb} and present the results in Table 2. The value of $\mathcal{R}$ increases since R_{Qb} is shorter than R_{mean}. All the galaxies move to the fast regime, except for NGC 6497. We discuss this galaxy later and conclude it does not host an ultrafast bar. In addition, the bars of IC 1683 and NGC 36 are consistent with being slow.

3.4. Comparison of bar radius estimates

We measured R_{bar} in the sample galaxies with three more methods based on the ellipse fitting and Fourier analysis of the deprojected images, as done by Lee et al. (2019, 2020). In particular, we calculated R_ϵ and R_{tran} from the ellipticity and PA radial profiles of the deprojected SDSS i-band images, as the radius where the maximum of ϵ occurs and where the PA varies by 2° with respect to the location of the peak in ϵ, respectively, and R_{A_2} as the radius corresponding to the maximum value of the amplitude A_2 of the Fourier $m = 2$ component, in the region where the phase angle ϕ_2 remains constant. We compare the new R_{bar} estimates with those obtained with similar methods by Aguerri et al. (2015) and Cuomo et al. (2019b) in Fig. 4. In particular, we put R_ϵ together with $R_{\epsilon,peak}$, R_{tran} with R_{PA}, and R_{A_2} with $R_{Fourier}$. While $R_{\epsilon,peak} \sim R_\epsilon$, and $R_{PA} \sim R_{tran}$ although with some scatter, it results that systematically $R_{Fourier} > R_{A_2}$. This discrepancy is due to the slightly different definition of R_{bar} in the two Fourier-based methods. In fact, R_{A_2} considers the peak of the $m = 2$ component of the Fourier series in the region in which ϕ_2 remains constant to exclude the range with higher peaks in the Fourier $m = 2$ component caused by spiral arms. On the other, hand, $R_{Fourier}$ requires the higher orders of the Fourier series and does not include the behaviour of the corresponding phase angles. The even components of the Fourier series, together with the corresponding phase angles and in particular the $m = 2$ one, can be strongly affected
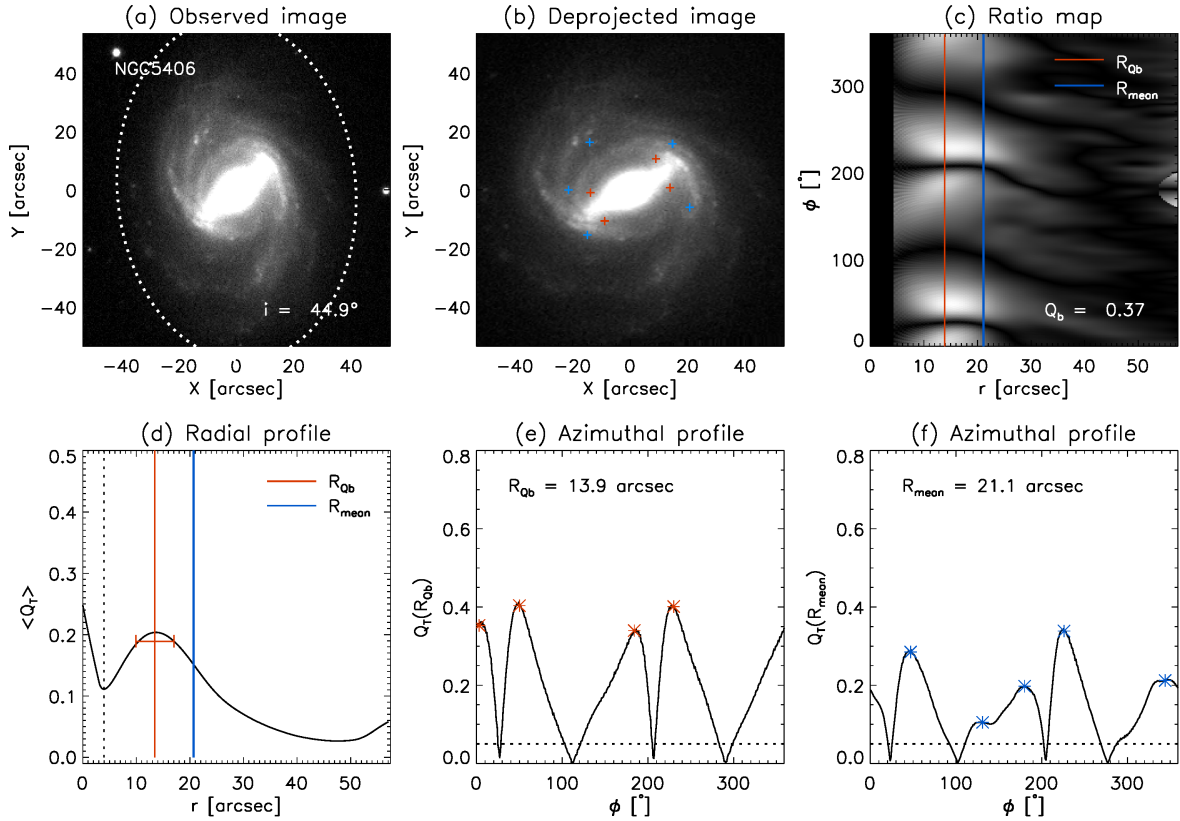
Fig. 3. Analysis of the ratio map of NGC 5406. *Panel a*: observed *i*-band SDSS image of the galaxy with north up and east left. The dotted ellipse indicates the region of the galaxy considered for the deprojection. The galaxy inclination is given. *Panel b*: deprojected image of the galaxy. The red and blue crosses correspond to the peaks measured in the $Q_T(R_{Qb})$ and $Q_T(R_{mean})$ azimuthal profiles, respectively. *Panel c*: map of the transverse-to-radial force ratio $Q_T(r, \phi)$. The vertical blue and red lines indicate the location of R_{Qb} and R_{mean}, respectively. The bar strength is given. *Panel d*: radial profile of $\langle Q_T \rangle$. The vertical dotted line corresponds to the boundary of the bulge-dominated region, identified as the range from the centre to the minimum (or a change in the slope) in the $\langle Q_T \rangle$ radial profile. The vertical blue and red lines indicate the location of R_{Qb} and R_{mean}, respectively. The horizontal red segment represents the error associated with R_{Qb}. *Panel e*: azimuthal profile of $Q_T(R_{Qb})$. The local maxima of the profile are highlighted by red asterisks. The horizontal dotted line corresponds to the threshold value at $Q_T = 0.05$, adopted to count the number of peaks associated with the bar. The value of R_{Qb} from this paper is given. *Panel f*: azimuthal profile of $Q_T(R_{mean})$. The local maxima of the profile are highlighted by blue asterisks. The horizontal dotted line corresponds to the threshold value at $Q_T = 0.05$, adopted to count the number of peaks associated with the bar. The value of R_{mean} from literature is given.

by the prominence of the bulge (Debattista et al. 2002a; Lee et al. 2020).

In Fig. 5 we compare all the different R_{bar} estimates of the sample galaxies to R_{Qb} as well as their mean value R_{mean} given in Table 1. We note that R_{Qb} is systematically shorter than R_{mean} and the other available measurements of R_{bar}. In particular, R_{Qb} is always shorter than R_{mean} at face values, but for three galaxies the two R_{bar} estimates are consistent within the errors. This is due to the large errors associated with R_{mean}. The difference between R_{mean} and R_{Qb} increases for the longer bars of the sample, such as those residing in IC 1683, NGC 36, NGC 2553, and NGC 5406. Our findings are in agreement with those of Lee et al. (2020) who compared their measurements of R_{bar} in sample of about 400 spiral galaxies with those available in literature (Laurikainen & Salo 2002; Díaz-García et al. 2016) and found a strong correlation between R_{A_2} and R_{Qb}.

As a consequence of the trends shown in Fig. 5, we can conclude that the various estimates of R_{bar} generally lead to smaller values of $\mathcal{R}$ with respect to R_{Qb}, although a solid estimate of the errors on R_{bar} is not available so far for all the measurement methods. The values of $\mathcal{R}$ derived for R_{mean} and R_{Qb} are given in Tables 1 and 2, respectively, while the values of $\mathcal{R}$ from $R_{\epsilon,peak}$, R_{PA}, $R_{Fourier}$, R_{ϵ}, R_{tran}, and R_{A_2} are reported in Table B.1.

3.5. Results for individual galaxies

We performed the morphological classification of the sample galaxies following the criteria given by Buta et al. (2015), Buta (2017), and Bittner et al. (2020).

IC 1528. A flocculent galaxy with strong spiral arms and no rings. Owing to its high inclination ($i \sim 70°$), we cannot understand whether it is an unbarred galaxy, where the bar is mimicked by the winding spiral arms, or a genuine weakly barred galaxy, as suggested by the weak four peaks in the $Q_T(R_{Qb})$ azimuthal profile. The ratio map does not present the typical four slabs for barred galaxies and there is no peak or plateau in the $\langle Q_T \rangle$ radial profile. Therefore, we excluded IC 1528 from the discussion related to the analysis of the ratio maps.

IC 1683. A two-armed spiral galaxy without rings, which we classified to belong to the (*s*) variety with arms breaking out directly from the bar. The ratio map presents four slabs for $r \lesssim 35$ arcsec and an outer complex pattern corresponding to the spiral arms. The $\langle Q_T \rangle$ radial profile decreases till a local minimum at $r = 4.0$ arcsec in the bulge region, then it increases to a maximum value at R_{Qb}. The corresponding $Q_T(R_{Qb})$ azimuthal profile presents four peaks with $Q_b = 0.28$. The $Q_T(R_{mean})$
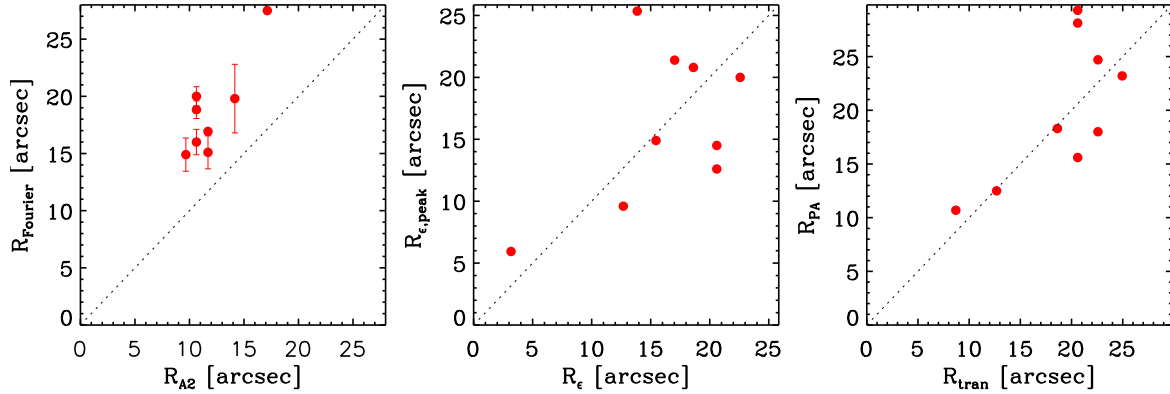
Fig. 4. Comparison between the bar radius of the sample galaxies obtained with similar methods based on Fourier analysis (*left panel*), ellipticity (*central panel*), and PA (*right panel*) radial profiles.

azimuthal profile shows four weaker peaks. The value of R_{mean} is larger than R_{Qb} and they are not consistent with each other.

IC 5309. An inclined spiral galaxy with strong grand-design spiral arms but no rings. The ratio map presents four slabs for $r \lesssim 10$ arcsec and an outer complex pattern corresponding to the spiral arms. The $\langle Q_{\mathrm{T}} \rangle$ radial profile is dominated by the bulge till $r = 2.8$ arcsec and then decreases to a kind of a plateau, corresponding to the four peaks in the $Q_{\mathrm{T}}(R_{\mathrm{Qb}})$ azimuthal profile. We classified the galaxy as weakly barred for its low bar strength $Q_b = 0.11$. The $Q_{\mathrm{T}}(R_{\mathrm{mean}})$ azimuthal profile presents only three peaks. The values of R_{mean} and R_{Qb} are consistent within the errors.

NGC 36. A grand-design spiral galaxy with a inner ring and an outer pseudo-ring, which we highlighted by adopting the (r) and (R'_2) varieties for the morphological classification. The ratio map presents four slabs extending to the outer regions of the galaxy and corresponding to both the bar and inner ring. The $\langle Q_{\mathrm{T}} \rangle$ radial profile decreases to a local minimum at $r = 4.0$ arcsec in the bulge region, then it increases to a maximum value at R_{Qb}. The corresponding $Q_{\mathrm{T}}(R_{\mathrm{Qb}})$ azimuthal profile presents four peaks with $Q_b = 0.33$. The $Q_{\mathrm{T}}(R_{\mathrm{mean}})$ azimuthal profile shows four peaks, even if they are less prominent. The size of the inner ring corresponds to R_{mean}, which is not consistent with R_{Qb}.

NGC 2553. A two-armed spiral, which we recognize to have an inner (r) and an outer $(R_1 R'_2)$ morphology. The ratio maps present four well-defined slabs extending to the outer regions of the galaxy. The $\langle Q_{\mathrm{T}} \rangle$ radial profile decreases to a local minimum at $r = 3.6$ arcsec in the bulge region, then it increases till a maximum value at R_{Qb}. The corresponding $Q_{\mathrm{T}}(R_{\mathrm{Qb}})$ azimuthal profile presents four peaks with $Q_b = 0.26$. The $Q_{\mathrm{T}}(R_{\mathrm{mean}})$ azimuthal profile shows six weak peaks. The size of the inner ring corresponds to R_{mean}, which is consistent with R_{Qb} within the errors.

NGC 2880. The only lenticular galaxy of the sample. It hosts a large bulge and a bar almost aligned with the disc minor axis. The ratio map presents four well-defined slabs extending to the outer regions of the galaxy. The $\langle Q_{\mathrm{T}} \rangle$ radial profile decreases to a local minimum at $r = 6.0$ arcsec in the bulge region. Then, the $\langle Q_{\mathrm{T}} \rangle$ radial profile increases to a plateau corresponding to the four peaks in the $Q_{\mathrm{T}}(R_{\mathrm{Qb}})$ azimuthal profile with $Q_b = 0.19$. The $Q_{\mathrm{T}}(R_{\mathrm{mean}})$ azimuthal profile shows the same four peaks. The values of R_{mean} and R_{Qb} are consistent within the errors.

NGC 5205. A multiple-armed spiral galaxy with an inner broken ring, which we translated into an (rs) classification. The

ratio map presents four slabs for $r \lesssim 30$ arcsec and an outer complex pattern corresponding to the spiral arms. The $\langle Q_{\mathrm{T}} \rangle$ radial profile decreases to a local minimum at $r = 5.9$ arcsec in the bulge region, then this radial profile increases to a maximum value at R_{Qb}. The corresponding $Q_{\mathrm{T}}(R_{\mathrm{Qb}})$ azimuthal profile presents four peaks with $Q_b = 0.29$. The peaks are nearly the same in the $Q_{\mathrm{T}}(R_{\mathrm{mean}})$ azimuthal profile. The size of the inner broken ring corresponds to R_{mean}, which is consistent with R_{Qb} within the errors.

NGC 5406. A multiple-armed spiral galaxy with an inner broken ring and an (rs) morphology. The ratio map presents four slabs for $r \lesssim 25$ arcsec and an outer complex pattern corresponding to the spiral arms. The $\langle Q_{\mathrm{T}} \rangle$ radial profile decreases to a local minimum at $r = 4.4$ arcsec in the bulge region and then increases till a maximum value at R_{Qb}. The corresponding $Q_{\mathrm{T}}(R_{\mathrm{Qb}})$ azimuthal profile presents four peaks with $Q_b = 0.37$. The value of R_{mean} corresponds to the ring size and the presence of a spiral arm in the ring region gives rise to the fifth peak observed in the $Q_{\mathrm{T}}(R_{\mathrm{Qb}})$ azimuthal profile. The values of R_{mean} and R_{Qb} are consistent within the errors.

NGC 5947. A multiple-armed spiral galaxy. We note the presence of an inner ring, which translates into an (r) classification. The ratio map presents four slabs for $r \lesssim 20$ arcsec and an outer complex pattern corresponding to the spiral arms. The $\langle Q_{\mathrm{T}} \rangle$ radial profile decreases to a local minimum at $r = 2.8$ arcsec in the bulge region and then increases to a maximum value at R_{Qb}. The corresponding $Q_{\mathrm{T}}(R_{\mathrm{Qb}})$ azimuthal profile presents four peaks with $Q_b = 0.26$. The $Q_{\mathrm{T}}(R_{\mathrm{mean}})$ azimuthal profile is characterised by four peaks too. The size of the ring corresponds to R_{mean}, which is consistent with R_{Qb} within the errors.

NGC 5971. An highly inclined spiral galaxy ($i \sim 70°$) with multiple arms. Its deprojection produces an artefact bar structure along the disc minor axis hampering the analysis of the ratio map, which nevertheless shows the typical four slabs associated with a bar. We excluded NGC 5971 from the discussion related to the analysis of the ratio maps.

NGC 6497. A multiple-armed spiral galaxy with flocculent spiral arms. We translated the presence of outer rings into an $(R_1 R'_2)$ morphology. The ratio map presents four slabs for $r \lesssim 15$ arcsec. The $\langle Q_{\mathrm{T}} \rangle$ radial profile decreases to a local minimum at $r = 3.6$ arcsec in the bulge region and then increases to a maximum value at R_{Qb}. The corresponding $Q_{\mathrm{T}}(R_{\mathrm{Qb}})$ azimuthal profile presents four peaks with $Q_b = 0.34$. The same peaks
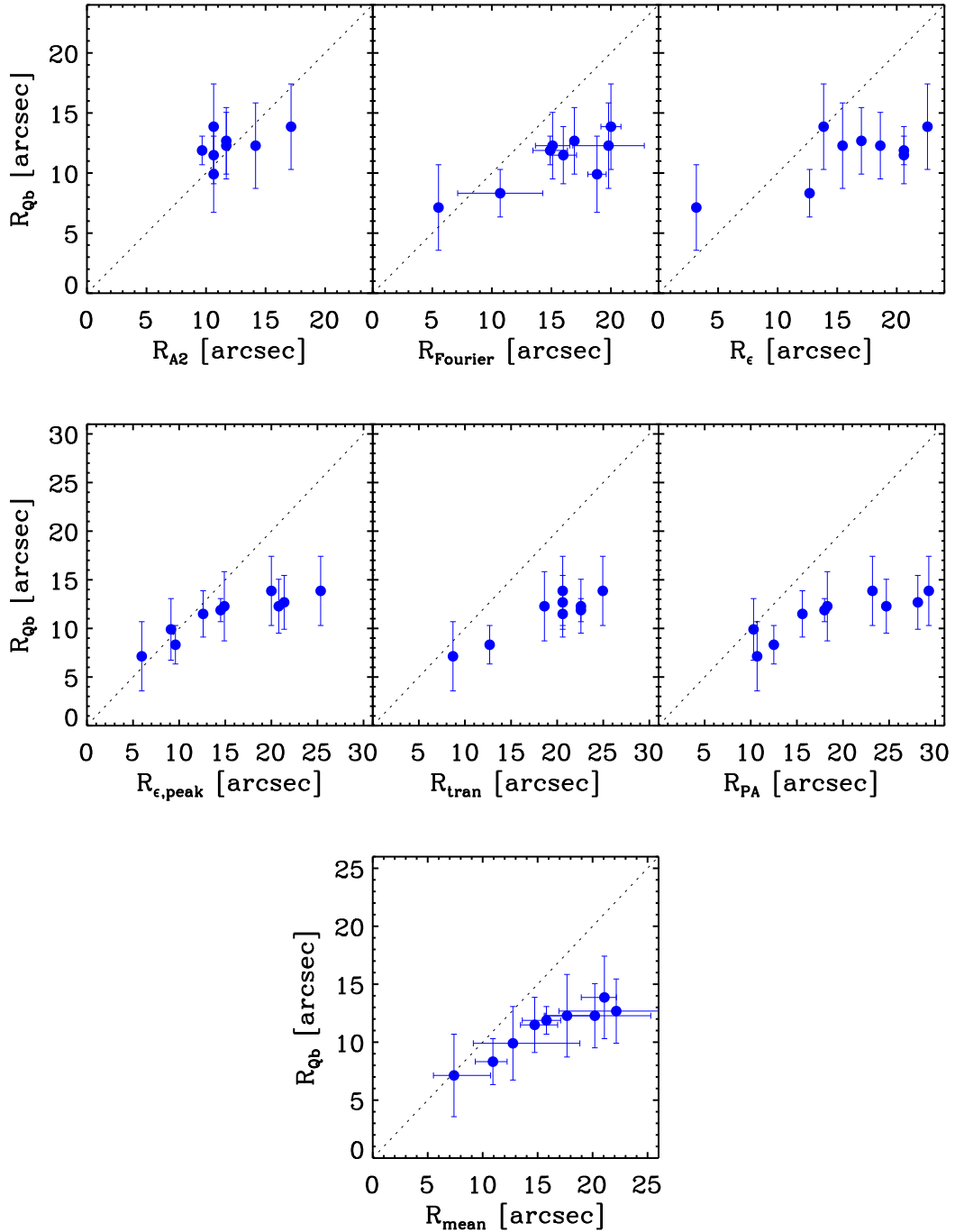
Fig. 5. Comparison between the bar radius of the sample galaxies obtained with several methods and the analysis of the ratio maps. *Lower panel*: comparison between R_{mean} and R_{Qb} given in Tables 1 and 2, respectively.

are shown by the $Q_T(R_{mean})$ azimuthal profile. The ring size is consistent with R_{mean}, which agrees with R_{Qb} within the errors.

UGC 3253. A multiple-armed spiral galaxy. The presence of an inner ring translates into an (r) classification. The ratio map presents four slabs for $r \lesssim 20$ arcsec and an outer complex pattern corresponding to the spiral arms. The $\langle Q_T \rangle$ radial profile decreases to a local minimum at $r = 4.0$ arcsec in the bulge region and then increases to a maximum value at R_{Qb}. The corresponding $Q_T(R_{Qb})$ azimuthal profile presents four peaks with $Q_b = 0.40$. The $Q_T(R_{mean})$ azimuthal profile shows the same peaks. The size of the inner ring corresponds to R_{mean}, which is consistent with R_{Qb} within the errors.

4. Discussion

The bars of a number of disc galaxies of the CALIFA survey with direct and accurate measurements of Ω_{bar} are characterised by $\mathcal{R} < 1$ (Aguerri et al. 2015; Cuomo et al. 2019a). These unexpected observational findings are dynamically incompatible with the theoretical predictions about the stability of stellar orbits supporting the bar (Contopoulos 1981). Therefore, we decided to test whether these ultrafast bars are an artefact due to an overestimated value of R_{bar} and/or an underestimated value of R_{cr} rather than a new class of non-axisymmetric stellar components, whose orbital structure has not been yet understood.

For all the sample galaxies, we find that the R_{bar} measurement based on the analysis of the ratio maps is shorter than

that obtained with other methods based on ellipse fitting and Fourier analysis of the deprojected galaxy image. These methods turned out to be very sensible to the presence of rings, pseudo-rings, and spiral arms, which are very common in the galaxies we analysed and lead to systematically larger values of R_{bar}. All the sample galaxies present a rather complex spiral morphology, except for NGC 2880. This is a lenticular galaxy, which does not show any additional component to the bulge, bar, and disc and its R_{Qb} is consistent (although smaller) with R_{bar} derived from other methods.

When adopting R_{Qb} to calculate $\mathcal{R}$, all the galaxies turned out to host a fast bar at 95% confidence level with the only exception represented by NGC 6497. This galaxy was previously discussed in detail by Aguerri et al. (2015) and Garma-Oehmichen et al. (2020). Aguerri et al. (2015) analyse the galaxy extinction map to rule out problems in measuring R_{bar} due to dust and consider the gas kinematics to check V_{circ} and hence R_{cr} obtain from stellar dynamics. Garma-Oehmichen et al. (2020) reassess the error budget of Ω_{bar} by considering a broader set of error sources affecting the TW method. They remeasure Ω_{bar} and recalculat R_{cr}; they obtain $\mathcal{R} = 1.08^{+0.31}_{-0.25}$, which makes NGC 6497 fully consistent with the fast-bar regime.

Our results of the problems in measuring R_{bar} in barred galaxies confirm previous findings based on the analysis of mock images and numerical simulations. Michel-Dansac & Wozniak (2006) showed that $\mathcal{R}$ can increase from 1.0 to 1.4 just by changing the method adopted to recover R_{bar}. Using simulated images, they showed that R_{bar} obtained from the location of the maximum in the ϵ radial profile is closer to R_{cr}, whereas R_{bar} estimated from the location of the constant PA or from the Fourier analysis correlates with the ultra-harmonic 4:1 resonance well within R_{cr}. Different R_{bar} values translate into different $\mathcal{R}$ estimates. More recently, Petersen et al. (2019) show with N-body simulations that R_{bar} measured from ellipse fitting overestimates by a factor 1.5–2 the radial extent of the bar recovered from the maximum excursion of x_1 stellar orbits. This is because many untrapped stellar orbits reside in the physical regions of the x_1 family and are considered part of the bar by the ellipse fitting.

Using the images of mock galaxies, Lee et al. (2020) show that the measurement of R_{bar} based on the ratio map are overestimated when the bulge-to-total ratio B/T increases from 0 to 0.8, but the same effect is pointed out for the ellipse fitting and Fourier analysis methods as well. This means that if there is a substantial contribution of the bulge, the corresponding rotation rate is more effectively driven out the ultrafast regime into the fast regime. The bulges in our galaxies give a relatively low contribution to the total luminosity, with a mean value of $\langle B/T \rangle = 0.15$ (Méndez-Abreu et al. 2017), when excluding the SB0 NGC 2880, which hosts a large bulge ($B/T = 0.46$). More-over, the ratio map allows us to disentangle the radius corresponding to the maximum strength of the bar from that of the spiral arms and/or rings by comparing the $Q_T(R_{Qb})$ and $Q_T(R_{mean})$ azimuthal profiles and looking at where the local maxima of the azimuthal profiles are located in the image of the galaxy. For a future perspective, it is worth checking whether bars located in the safe fast regime are in turn affected by a wrong estimate of bar radius, especially when the host galaxies present spiral arms and/or rings. If this is the case, some of those bars may belong to the slow regime, challenging the conclusions drawn so far in the framework of bar rotation regimes. Unfortunately, all the most widely adopted methods to recover R_{bar} are based only on photometry without considering kinematic information, which may help to successfully constrain the extension of the bar.

Hilmi et al. (2020) use hydro-dynamical simulations of Milky Way-like galaxies to assess the variation of the bar parameters on a dynamical timescale owing to the interaction with the spiral structure. Using different approaches based on photometry, these authors recover R_{bar}, S_{bar}, and Ω_{bar} and trace their evolution with time. All the adopted methods overestimate R_{bar}. The bar rotates faster than the spiral pattern and sometimes bar and spiral arms overlap. When the bar is connected to spiral arms, it seems to increase its radius. These bar pulsations are due to the coupling with the modes of the spiral pattern. Since the spiral modes can be odd, the two bar ends typically do not connect at exactly the same time to a spiral arm, so the two bar radii (one per each half) may be different at some given time. According to Hilmi et al. (2020), in ∼50% of Milky Way-like galaxies, the R_{bar} measurements of SBab and SBbc galaxies are overestimated by ∼15% and ∼55%, respectively, where the stronger bars drive larger errors. Considering the sample analysed by Cuomo et al. (2020), we point out that ultrafast bars seem to be associated with stronger bars only when galaxies with TW measurements are considered. We find that R_{Qb} values are on average ∼45% shorter than other R_{bar} estimates for our sample galaxies and that this difference decreases from SBab to SBc galaxies. Moreover, Hilmi et al. (2020) show that while the bar is increasing its radius owing to the interaction with the spiral structure, the corresponding Ω_{bar} decreases, but at a lower rate. Therefore, the two effects do not cancel out: intrinsically fast bars may appear as ultrafast. Given that Ω_{bar} is well determined in our sample galaxies with the TW method, finding ultrafast bars need to be associated with an erroneous determination of R_{bar}.

It should be noted that it is mandatory to adopt the same approach in measuring R_{bar} when the theoretical predictions (Weinberg 1985; Hernquist & Weinberg 1992) and numerical simulations (Debattista & Sellwood 2000; Zou et al. 2019; Ghafourian et al. 2020) are compared to observational results to avoid misinterpreting the data. On the other hand, $\mathcal{R}$ also depends on R_{cr} and hence on Ω_{bar} and V_{circ}. Aguerri et al. (2015) and Cuomo et al. (2019a) derive V_{circ} from the asymmetric drift-corrected stellar kinematics in the disc region (Binney & Tremaine 2008) and verify that their values agree with the Tully-Fisher relation predictions (Tully & Fisher 1977; Reyes et al. 2011). Moreover, Aguerri et al. (2015) recover V_{circ} for NGC 36, NGC 5205, and NGC 6497 using available gas kinematics (Theureau et al. 1998; ?) and exclude in these cases the determination of V_{circ} can explain the observed ultrafast regime. On the other hand, Garma-Oehmichen et al. (2020) directly estimate the value of R_{cr} as the intersection between Ω_{bar} and the modelled angular rotation curve, which is useful for galaxies where the rotation curve rises slowly and R_{cr} can be overestimated when measured using V_{circ}, but they do not infer any conclusion about the ultrafast regime.

In this paper, we consider only ultrafast barred galaxies with a direct measurement of Ω_{bar} from the TW method. We already discussed the sources of error of the TW method in Sect. 3, but some further considerations are worth bearing in mind.

Using N-body simulations, Zou et al. (2019) suggest that $\mathcal{R} < 1$ can occur when ΔPA between bar and disc major axes is overestimated, the bar is too close to the disc minor axis, and the field of view is too small to guarantee the convergence of the TW integrals. In addition, Cuomo et al. (2019b) show that $\mathcal{R} < 1$ could also be the result of a wrong estimate of the disc PA from ellipse fitting when the PA radial profile is not constant as for warped discs. All the findings imply that ultrafast bars could be due to a wrong application of the TW method. However, we

exclude this is the case for our sample galaxies, which were carefully selected to be perfectly suitable for the correct application of the TW technique. As detailed by Aguerri et al. (2015) and Cuomo et al. (2019a), in performing their TW measurements, the PA of the bar and of the disc major axes were carefully measured with an ellipse fitting analysis; the constant portion of the PA profile, corresponding to the disc region in which the bar is located, was identified; no correlation was found between the relative errors of R_{cr} and R_{bar} and the values of the disc i and bar ΔPA with respect to the disc major axis; and the radial extent of the photometric and kinematic data was chosen to allow the convergence of the TW integrals.

The existence of distinct pattern speeds corresponding to different galaxy structures has been extensively discussed (Rautiainen et al. 2008; Cuomo et al. 2019a). There have been some efforts to modify and apply the TW method to recover multiple pattern speeds. The assumption of a well-defined rigidly rotating pattern speed in a barred galaxy can be questioned in the case of rings and/or spiral arms. The bar and spiral arms possibly share the same pattern speed when the arms are driven by the bar (Sanders & Huntley 1976), or the bar and spiral arms can have different pattern speeds even if they are connected (Sellwood & Sparke 1988; Beckman et al. 2018; Hilmi et al. 2020). Moreover, these pattern speeds may vary in space and/or time (Toomre et al. 1981; Bertin & Lin 1996). The TW method provides an average pattern speed, if multiple pattern speeds are present. Since the length of the pseudo-slits must reach the axisymmetric disc, crossing the bar and the spiral arms is unavoidable. As already pointed out by Tremaine & Weinberg (1984), Debattista et al. (2002b) show that small perturbations in the disc density do not contribute significantly to Ω_{bar}. Low amplitudes correspond to a rapidly growing structure, which corresponds to spiral arms. Meidt et al. (2008) adapt the TW method to measure different pattern speeds from independent radial regions. They argue that for spiral galaxies as well, the bar contribution to the measured pattern speed is maximal when only the photometric and kinematic integrals taken across the bar are considered in the analysis. This is commonly done in the application of the TW method to spiral galaxies (Aguerri et al. 2015; Cuomo et al. 2019a; Guo et al. 2019; Garma-Oehmichen et al. 2020; Williams et al. 2021). In this case, the measured pattern speed is reliable (Meidt et al. 2008). Moreover, deviations from the bar pattern speed are small when the spiral arms are dim (Williams et al. 2021). A slope change of the straight-line fitting the TW integrals was also interpreted as the signature of a nuclear bar rotating with a different pattern speed with respect to the main bar (Corsini et al. 2003; Maciejewski 2006; Meidt et al. 2009). A slight slope change is observed in some of the galaxies of our sample as well as in other galaxies that do not host an ultrafast bar (Aguerri et al. 2015; Cuomo et al. 2019a), so we can conclude there is no clear link between the originally observed ultrafast regime and the slope change.

Dark gaps are commonly seen in early- to intermediate-type barred galaxies having inner and outer rings or related features: the radial zone between an inner and outer ring appears dark, either continuously or in 2–4 distinct sections (Kim et al. 2016; James & Percival 2016; Buta 2017). Buta (2017) suggest that the dark gaps between inner and outer rings are associated with the L_4 and L_5 Lagrangian points in the gravitational potential of a bar or an oval. In turn, these points are theoretically expected to lie very close to the corotation resonance of the bar pattern, so the gaps may provide the location of R_{cr}. According to Kim et al. (2016), the inner disc stars are swept by the bar and thus sparse regions are thought to be produced by the bar driven secular evo-

lution. Pronounced light deficits are expected to be observed as the bar evolves becoming more extended and stronger. During the evolution of a barred galaxy, the bar loses angular momentum by trapping nearby disc stars onto elongated orbits. This results in an increase in the bar radius and strength (Athanassoula & Misiriotis 2002; Athanassoula et al. 2013; Kim et al. 2016). Buta (2017) find a mean bar rotation rate $\langle \mathcal{R} \rangle = 1.58 \pm 0.04$ for a sample of 50 galaxies with dark gaps and this means that they host slow-rotating bars. Measuring $\mathcal{R} < 1$ in galaxies with dark gaps reinforces the idea that ultrafast bars are due to an artefact in the determination of the rotation rate. Our analysis moves ultrafast bars into the fast (and even in the slow) regimes, which agrees with the expected results for evolved galaxies with dark gaps.

However, Buta (2017) identify a sub-class of dark gaps, where the interior of an inner ring appears darker than outside. He found a redder colour in the dark gaps with respect to the bars and no recent star formation. This agrees with the scenario of a bar depleting nearby regions from stars, while evolving. On the other hand, the rotation rates seem to locate these bars in the ultrafast regime. Buta (2017) claims that if the dark spaces in these galaxies are interpreted in the same way as for the inner/outer ring gap galaxies, then either the existence of ultrafast bars would have to be acknowledged or another mechanism for forming dark gaps that has nothing to do with Lagrangian points would have to be hypothesised. This specific morphology can be recognised in two of our galaxies, NGC 5406 and NGC 5947. Since we excluded that the analysed bars are rotating extremely fast, we stress a different mechanism is needed to explain at least this sub-class of galaxies with dark gaps.

5. Conclusions

In this paper we considered the case of ultrafast bars, which are observed in more than 10% of barred galaxies with a direct measurement of the bar pattern speed. These bars end beyond the corotation radius and therefore challenge our understanding of stellar dynamics in barred galaxies. We aimed to investigate whether ultrafast bars are an artefact due to an overestimated value of R_{bar} and/or an underestimated value of R_{cr} rather than a new class of non-axisymmetric stellar components, whose orbital structure has not been yet understood.

We took into account the 12 barred galaxies, for which Ω_{bar} was carefully measured by applying the TW method to the integral-field spectroscopic data obtained by the CALIFA survey and which turned out to host an ultrafast bar according to its $\mathcal{R} < 1$ (Aguerri et al. 2015; Cuomo et al. 2019a).

We checked that the galaxies were selected to be suitable for the application of the TW method and confirmed the values obtained for their R_{cr}. Then, we analysed the issues related to the available R_{bar} measurements by Aguerri et al. (2015) and Cuomo et al. (2019a) based on the ellipse fitting and Fourier analysis of the deprojected SDSS i-band images of the sample galaxies. We also derived new estimates of R_{bar} from the analysis of the ϵ and PA radial profiles and of the Fourier $m = 2$ mode following the prescriptions of Lee et al. (2019, 2020).

We realised that nearly all the sample galaxies are spiral galaxies with an inner ring or pseudo-ring circling the bar and/or strong spiral arms, which hamper the R_{bar} measurements based on the ellipse fitting and Fourier analysis of the deprojected galaxy images. According to these methods, the ends of the ultrafast bars overlap with the inner ring and/or the spiral arms making the adopted R_{bar} unreliable.

Hence, we performed a further estimate of R_{bar} using the method proposed by Lee et al. (2020) and based on the analysis

of the ratio maps, which we successfully applied to ten galaxies. These values of R_{bar} are systematically smaller than R_{mean} and become smaller (or similar) to the corresponding R_{cr}. This implies that the corresponding $\mathcal{R}$ are larger than those obtained before. All the galaxies turned out host a fast bar at 95% confidence level with the only exception represented by NGC 6497. However, Garma-Oehmichen et al. (2020) recently recalculated R_{cr} for this galaxy and find this value is consistent with the fast-bar regime too.

We can confidently conclude that ultrafast bars are no longer observed when a correct measurement of R_{bar} is adopted. However, we are still missing a solid estimate of R_{bar} based on both photometric and kinematic data, unveiling the extension of the stellar orbits that support the bar and supporting the comparison with theoretical prescriptions and numerical simulations. This task requires further investigation.

References

Abazajian, K. N., Adelman-McCarthy, J. K., Agüeros, M. A., et al. 2009, ApJS, 182, 543
Abolfathi, B., Aguado, D. S., Aguilar, G., et al. 2018, ApJS, 235, 42
Adams, F. C., Ruden, S. P., & Shu, F. H. 1989, ApJ, 347, 959
Aguerri, J. A. L., Muñoz-Tuñón, C., Varela, A. M., & Prieto, M. 2000, A&A, 361, 841
Aguerri, J. A. L., Elias-Rosa, N., Corsini, E. M., & Muñoz-Tuñón, C. 2005, A&A, 434, 109
Aguerri, J. A. L., Méndez-Abreu, J., & Corsini, E. M. 2009, A&A, 495, 491
Aguerri, J. A. L., Méndez-Abreu, J., Falcón-Barroso, J., et al. 2015, A&A, 576, A102
Athanassoula, E. 1992, MNRAS, 259, 345
Athanassoula, E. 2003, MNRAS, 341, 1179
Athanassoula, E. 2014, MNRAS, 438, L81
Athanassoula, E., & Misiriotis, A. 2002, MNRAS, 330, 35
Athanassoula, E., Machado, R. E. G., & Rodionov, S. A. 2013, MNRAS, 429, 1949
Barazza, F. D., Jogee, S., & Marinova, I. 2008, ApJ, 675, 1194
Beckman, J. E., Font, J., Borlaff, A., & García-Lorenzo, B. 2018, ApJ, 854, 182
Bertin, G., & Lin, C. C. 1996, in Spiral Structure in Galaxies a Density Wave Theory
Binney, J., & Tremaine, S. 2008, Galactic Dynamics, 2nd edn. (Princeton, NJ, USA: Princeton University Press)
Bittner, A., Gadotti, D. A., Elmegreen, B. G., et al. 2020, in Galactic Dynamics in the Era of Large Surveys, eds. M. Valluri, & J. A. Sellwood, 353, 140
Bland-Hawthorn, J., & Gerhard, O. 2016, ARA&A, 54, 529
Buta, R. J. 2017, MNRAS, 470, 3819
Buta, R., & Block, D. L. 2001, ApJ, 550, 243
Buta, R. J., & Zhang, X. 2009, ApJS, 182, 559
Buta, R., Ryder, S. D., Madsen, G. J., et al. 2001, AJ, 121, 225
Buta, R. J., Sheth, K., Athanassoula, E., et al. 2015, ApJS, 217, 32
Combes, F., & Sanders, R. H. 1981, A&A, 96, 164
Comerón, S., Salo, H., Laurikainen, E., et al. 2014, A&A, 562, A121
Contopoulos, G. 1981, A&A, 102, 265
Contopoulos, G., & Grosbol, P. 1989, A&ARv, 1, 261
Contopoulos, G., & Papayannopoulos, T. 1980, A&A, 92, 33
Corsini, E. M. 2011, Mem. Soc. Astron. It. Suppl., 18, 23
Corsini, E. M., Debattista, V. P., & Aguerri, J. A. L. 2003, ApJ, 599, L29
Cuomo, V., Lopez Aguerri, J. A., Corsini, E. M., et al. 2019a, A&A, 632, A51
Cuomo, V., Corsini, E. M., Aguerri, J. A. L., et al. 2019b, MNRAS, 488, 4972
Cuomo, V., Aguerri, J. A. L., Corsini, E. M., & Debattista, V. P. 2020, A&A, 641, A111
Debattista, V. P. 2003, MNRAS, 342, 1194
Debattista, V. P., & Sellwood, J. A. 1998, ApJ, 493, L5
Debattista, V. P., & Sellwood, J. A. 2000, ApJ, 543, 704
Debattista, V. P., Corsini, E. M., & Aguerri, J. A. L. 2002a, MNRAS, 332, 65
Debattista, V. P., Gerhard, O., & Sevenster, M. N. 2002b, MNRAS, 334, 355
de Vaucouleurs, G., de Vaucouleurs, A., Corwin, H. G., Jr., et al. 1991, Third Reference Catalogue of Bright Galaxies (New York, USA: Springer-Verlag)
Díaz-García, S., Salo, H., & Laurikainen, E. 2016, A&A, 596, A84
Elmegreen, B. 1996, in Barred Galaxies, eds. R. Buta, D. A. Crocker, & B. G. Elmegreen (San Francisco, CA: Astron. Soc. Pac.), ASP Conf. Ser., 91, 197
Falcón-Barroso, J., Lyubenova, M., van de Ven, G., et al. 2017, A&A, 597, A48
Font, J., Beckman, J. E., Epinat, B., et al. 2011, ApJ, 741, L14
Friedli, D. 1999, in The Evolution of Galaxies on Cosmological Timescales, eds. J. E. Beckman, & T. J. Mahoney (San Francisco, CA: Astron. Soc. Pac.), ASP Conf. Ser., 187, 88
Fuchs, B. 2001, in Dark Matter in Astro- and Particle Physics, ed. H. V. Klapdor-Kleingrothaus, 25
Garcia-Lorenzo, B., Marquez, I., Barrera-Ballesteros, J. K., et al. 2015, VizieR Online Data Catalog: J/A+A/573/A59
Garma-Oehmichen, L., Cano-Díaz, M., Hernández-Toledo, H., et al. 2020, MNRAS, 491, 3655
Gerssen, J., & Debattista, V. P. 2007, MNRAS, 378, 189
Ghafourian, N., Roshan, M., & Abbassi, S. 2020, ApJ, 895, 13
Guo, R., Mao, S., Athanassoula, E., et al. 2019, MNRAS, 482, 1733
Hernquist, L., & Weinberg, M. D. 1992, ApJ, 400, 80
Hilmi, T., Minchev, I., Buck, T., et al. 2020, MNRAS, 497, 933
Hinshaw, G., Larson, D., Komatsu, E., et al. 2013, ApJS, 208, 19
James, P. A., & Percival, S. M. 2016, MNRAS, 457, 917
Jedrzejewski, R. I. 1987, MNRAS, 226, 747
Kim, T., Gadotti, D. A., Athanassoula, E., et al. 2016, MNRAS, 462, 3430
Kormendy, J. 1979, ApJ, 227, 714
Laurikainen, E., & Salo, H. 2002, MNRAS, 337, 1118
Lee, Y. H., Ann, H. B., & Park, M.-G. 2019, ApJ, 872, 97
Lee, Y. H., Park, M.-G., Ann, H. B., Kim, T., & Seo, W.-Y. 2020, ApJ, 899, 84
Lindblad, P. A. B., & Kristen, H. 1996, A&A, 313, 733
Little, B., & Carlberg, R. G. 1991, MNRAS, 251, 227
Maciejewski, W. 2006, MNRAS, 371, 451
Marinova, I., & Jogee, S. 2007, ApJ, 659, 1176
Martinez-Valpuesta, I., Aguerri, J. A. L., González-García, A. C., Dalla Vecchia, C., & Stringer, M. 2017, MNRAS, 464, 1502
Meidt, S. E., Rand, R. J., Merrifield, M. R., Debattista, V. P., & Shen, J. 2008, ApJ, 676, 899
Meidt, S. E., Rand, R. J., & Merrifield, M. R. 2009, ApJ, 702, 277
Méndez-Abreu, J., Ruiz-Lara, T., Sánchez-Menguiano, L., et al. 2017, A&A, 598, A32
Menéndez-Delmestre, K., Sheth, K., Schinnerer, E., Jarrett, T. H., & Scoville, N. Z. 2007, ApJ, 657, 790
Merrifield, M. R., & Kuijken, K. 1995, MNRAS, 274, 933
Michel-Dansac, L., & Wozniak, H. 2006, A, 452, 97
Morelli, L., Parmiggiani, M., Corsini, E. M., et al. 2016, MNRAS, 463, 4396
Noguchi, M. 1988, A&A, 203, 259
Ohta, K., Hamabe, M., & Wakamatsu, K.-I. 1990, ApJ, 357, 71
O'Neill, J. K., & Dubinski, J. 2003, MNRAS, 346, 251
Palunas, P., & Williams, T. B. 2000, AJ, 120, 2884
Petersen, M. S., Weinberg, M. D., & Katz, N. 2019, MNRAS, 490, 3616
Puerari, I., & Dottori, H. 1997, ApJ, 476, L73
Quillen, A. C., Frogel, J. A., & Gonzalez, R. A. 1994, ApJ, 437, 162
Rautiainen, P., Salo, H., & Laurikainen, E. 2008, MNRAS, 388, 1803
Reyes, R., Mandelbaum, R., Gunn, J. E., Pizagno, J., & Lackner, C. N. 2011, MNRAS, 417, 2347
Sánchez, S. F., Kennicutt, R. C., Gil de Paz, A., et al. 2012, A&A, 538, A8
Sanders, R. H., & Huntley, J. M. 1976, ApJ, 209, 53
Sanders, R. H., & Tubbs, A. D. 1980, ApJ, 235, 803
Sellwood, J. A. 1981, A&A, 99, 362
Sellwood, J. A. 2014, Rev. Mod. Phys., 86, 1
Sellwood, J. A., & Sparke, L. S. 1988, MNRAS, 231, 25
Starkman, N., Lelli, F., McGaugh, S., & Schombert, J. 2018, MNRAS, 480, 2292
Theureau, G., Bottinelli, L., Coudreau-Durand, N., et al. 1998, A&A, 130, 333
Toomre, A. 1981, in Structure and Evolution of Normal Galaxies, eds. S. M. Fall, & D. Lynden-Bell (Cambridge, UK: Cambridge University Press), Proc. Adv. Study Inst., 111
Tremaine, S., & Weinberg, M. D. 1984, ApJ, 282, L5
Tully, R. B., & Fisher, J. R. 1977, A&A, 500, 105
Vasiliev, E., & Athanassoula, E. 2015, MNRAS, 450, 2842
Villa-Vargas, J., Shlosman, I., & Heller, C. 2010, ApJ, 719, 1470
Walcher, C. J., Wisotzki, L., Bekeraité, S., et al. 2014, A&A, 569, A1
Weinberg, M. D. 1985, MNRAS, 213, 451
Williams, T. G., Schinnerer, E., Emsellem, E., et al. 2021, AJ, 161, 185
Wozniak, H., & Pierce, M. J. 1991, A&AS, 88, 325
Zhang, X., & Buta, R. J. 2007, AJ, 133, 2584
Zou, Y., Shen, J., Bureau, M., & Li, Z.-Y. 2019, ApJ, 884, 23

Appendix A: Analysis of the ratio maps for the entire sample

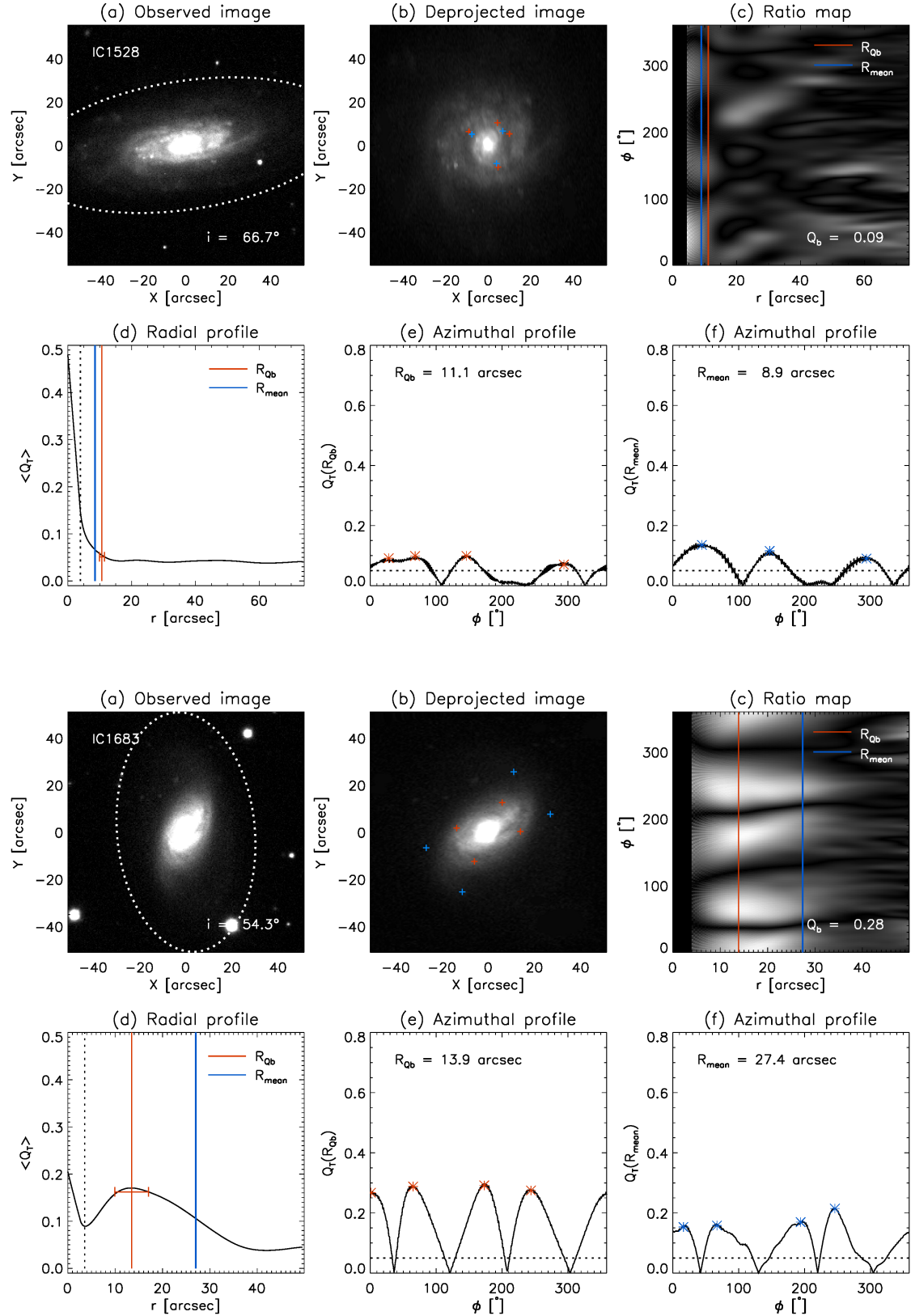We present the analysis of the ratio maps for the entire sample.

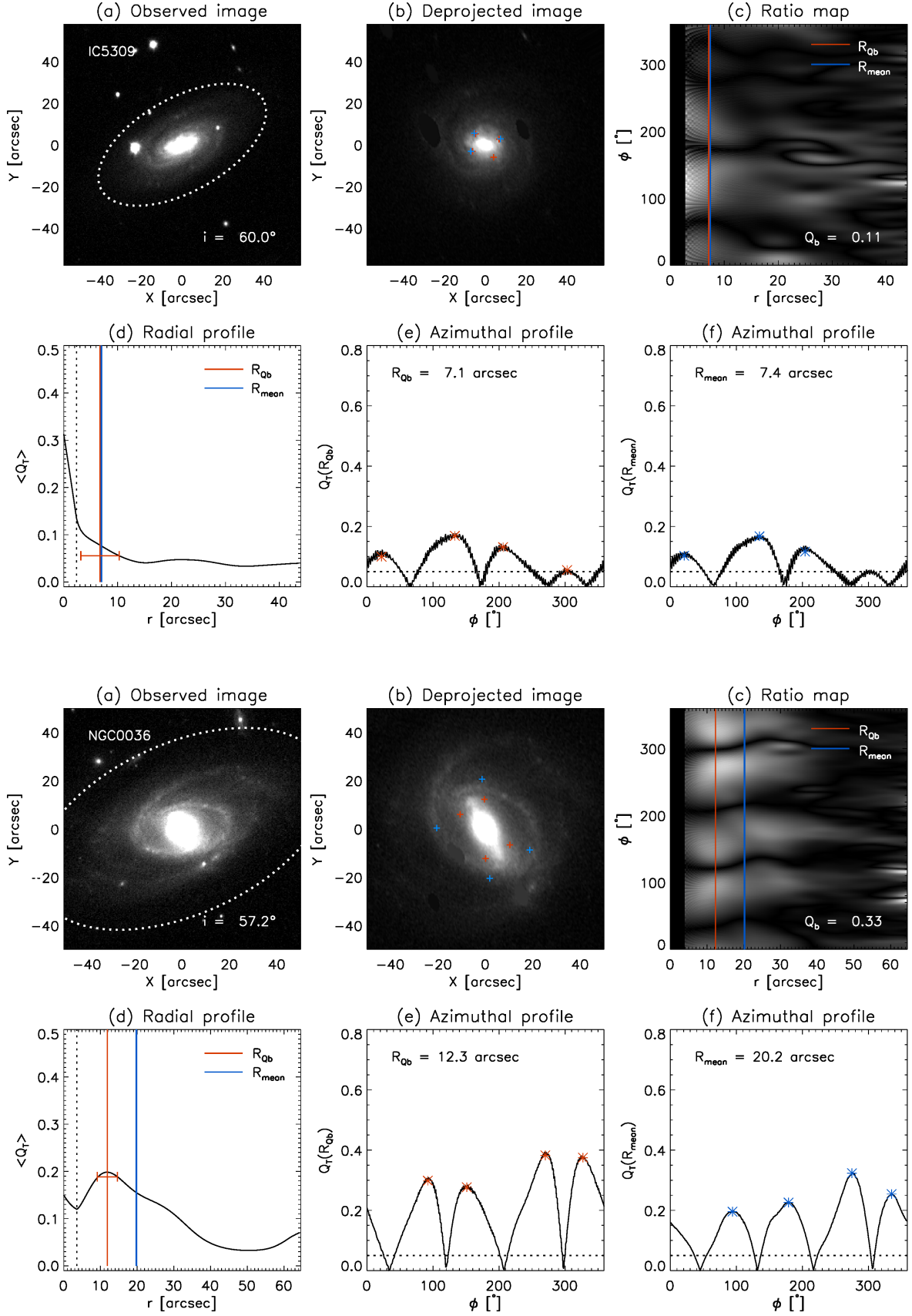**Fig. A.1.** Same as Fig. 3 but for the remaining galaxies of the sample.

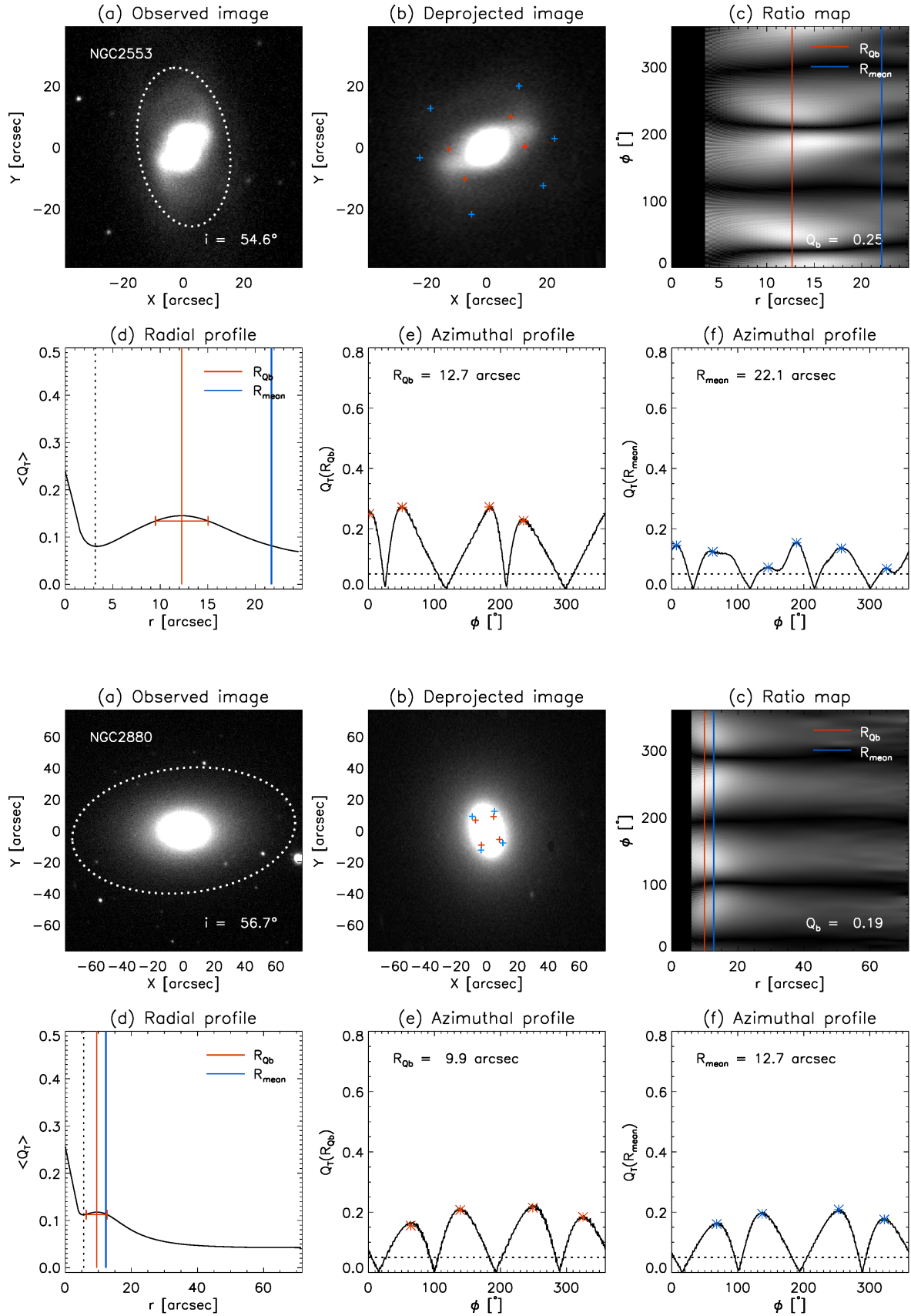**(a)** Observed image **(b)** Deprojected image **(c)** Ratio map

(d) Radial profile **(e)** Azimuthal profile **(f)** Azimuthal profile

Fig. A.1. continued.

(a) Observed image   **(b) Deprojected image**   **(c) Ratio map**

NGC2553

i = 54.6°

R_{Qb}

R_{mean}

Q_b = 0.25

(d) Radial profile   **(e) Azimuthal profile**   **(f) Azimuthal profile**

R_{Qb}

R_{mean}

R_{Qb} = 12.7 arcsec

R_{mean} = 22.1 arcsec

(a) Observed image   **(b) Deprojected image**   **(c) Ratio map**

NGC2880

i = 56.7°

R_{Qb}

R_{mean}

Q_b = 0.19

(d) Radial profile   **(e) Azimuthal profile**   **(f) Azimuthal profile**

R_{Qb}

R_{mean}

R_{Qb} = 9.9 arcsec

R_{mean} = 12.7 arcsec

Fig. A.1. continued.

Fig. A.1. continued.

(a) Observed image (b) Deprojected image (c) Ratio map
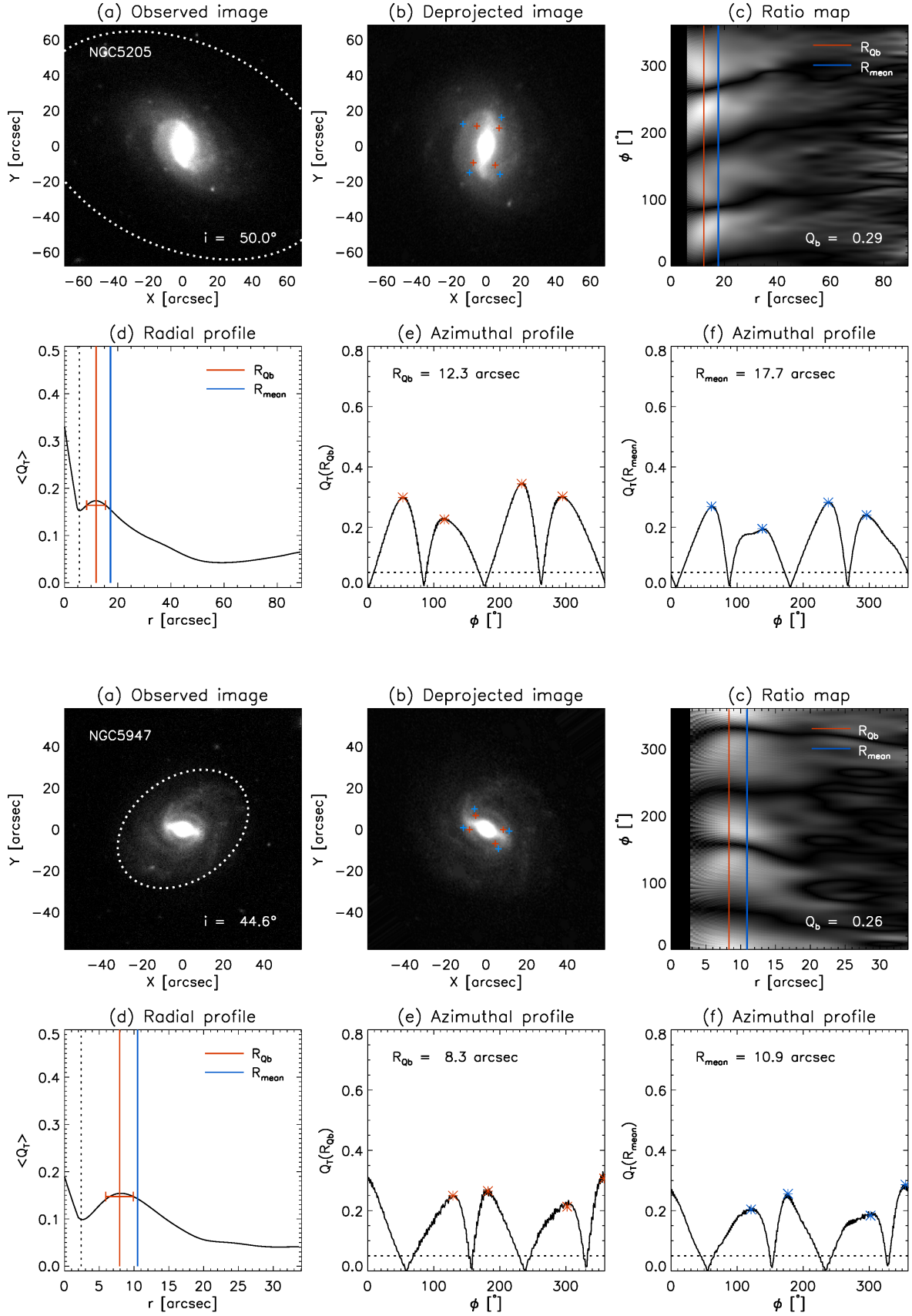### (d) Radial profile (e) Azimuthal profile (f) Azimuthal profile
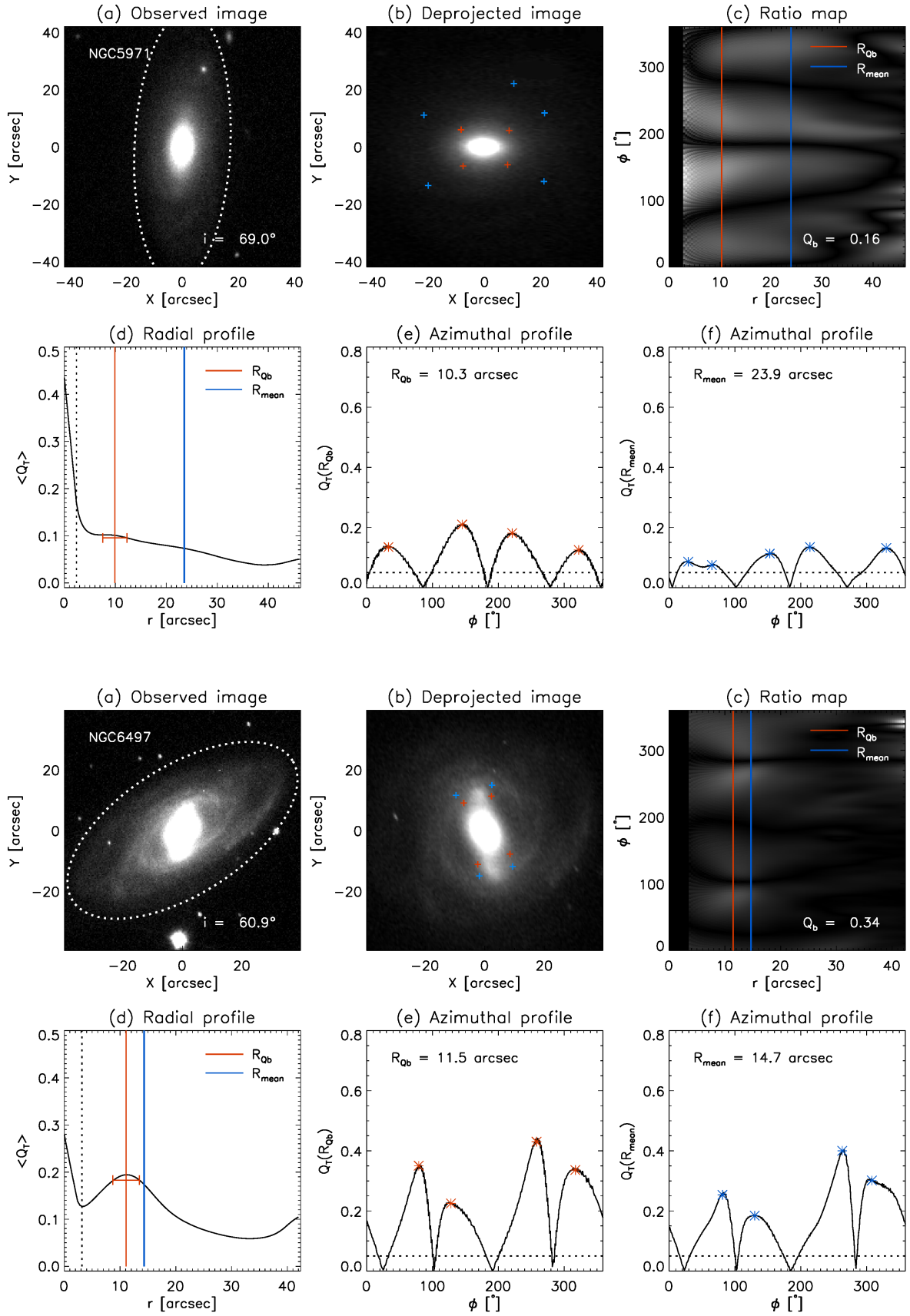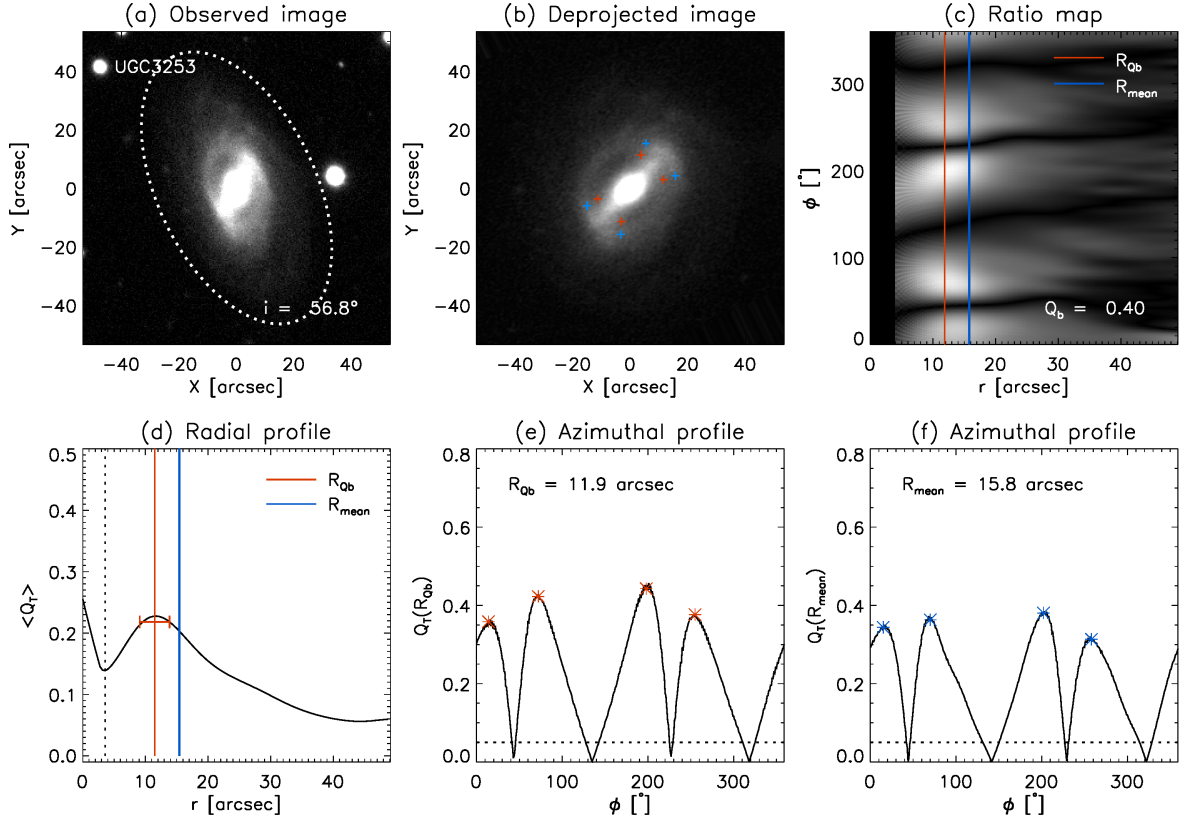
Fig. A.1. continued.

Fig. A.1. continued.

Appendix B: Bar rotation rates with different bar radius measurements

The measurements of $\mathcal{R}$ obtained with all the available estimates of $R_{\rm bar}$ are presented in Table B.1.

Table B.1. Bar rotation rates obtained with different bar radii.

Galaxy (1)	$\mathcal{R}_1$ (2)	$\mathcal{R}_2$ (3)	$\mathcal{R}_3$ (4)	$\mathcal{R}_4$ (5)	$\mathcal{R}_5$ (6)	$\mathcal{R}_6$ (7)
IC 1528	1.13	0.74	$0.58^{+0.17}_{-0.20}$	–	–	–
IC 1683	0.78	0.67	$0.72^{+0.35}_{-0.32}$	1.42	0.96	1.15
IC 5309	0.79	0.44	$0.85^{+0.73}_{-0.34}$	1.47	0.54	–
NGC 36	0.61	0.51	$0.83^{+0.33}_{-0.27}$	0.68	0.56	1.08
NGC 2553	0.53	0.41	$0.67^{+0.14}_{-0.14}$	0.67	0.55	0.97
NGC 2880	1.04	0.92	$0.50^{+0.16}_{-0.15}$	–	–	0.89
NGC 5205	0.76	0.61	$0.57^{+0.14}_{-0.13}$	0.73	0.61	0.80
NGC 5406	0.55	0.47	$0.55^{+0.21}_{-0.13}$	0.49	0.44	1.03
NGC 5947	0.60	0.46	$0.54^{+0.20}_{-0.26}$	0.46	0.46	–
NGC 5971	0.91	0.30	$1.03^{+0.50}_{-0.46}$	–	–	–
NGC 6497	0.44	0.35	$0.34^{+0.13}_{-0.11}$	0.27	0.27	0.52
UGC 3253	0.82	0.66	$0.80^{+0.21}_{-0.19}$	0.58	0.53	1.23

Notes. (1) Galaxy name. (2) Bar rotation rate obtained using $R_{\epsilon, \rm peak}$ as bar radius estimate. (3) Bar rotation rate obtained using $R_{\rm PA}$ as bar radius estimate. (4) Bar rotation rate obtained using $R_{\rm Fourier}$ as bar radius estimate. (5) Bar rotation rate obtained using R_{ϵ} as bar radius estimate. (6) Bar rotation rate obtained using $R_{\rm trann}$ as bar radius estimate. (7) Bar rotation rate obtained using $R_{\rm A_2}$ as bar radius estimate.